SANDIA REPORT

SAND2001-3675
Unlimited Release
Printed December 2001

Microscale Modeling and Simluation

Jim Redmond, Structural Dynamics Research; Dave Reedy, Material Mechanics; Martin Heinstein, Computational Solid Mechanics and Structural Dynamics; Maarten de Boer, MEMS Technology, Jim Knapp, Radiation Solid Interactions and Processing; Ed Piekos and Channy Wong, Microscale Science and Technology; Liz Holm, Materials and Process Modeling

Prepared by
Sandia National Laboratories
Albuquerque, New Mexico 87185 and Livermore, California 94550

Sandia is a multiprogram laboratory operated by Sandia Corporation, a Lockheed Martin Company, for the United States Department of Energy under Contract DE-AC04-94AL85000.

Issued by Sandia National Laboratories, operated for the United States Department of Energy by Sandia Corporation.

Available to DOE and DOE contractors from
U.S. Department of Energy
Office of Scientific and Technical Information
P.O. Box 62
Oak Ridge, TN 37831

Telephone: (865)576-8401
Facsimile: (865)576-5728
E-Mail: reports@adonis.osti.gov
Online ordering: http://www.doe.gov/bridge

Available to the public from
U.S. Department of Commerce
National Technical Information Service
5285 Port Royal Rd
Springfield, VA 22161

Telephone: (800)553-6847
Facsimile: (703)605-6900
E-Mail: orders@ntis.fedworld.gov
Online order: http://www.ntis.gov/ordering.htm

SAND2001-3675
Unlimited Release
Printed December 2001

Microscale Modeling and Simulation

Jim Redmond
Structural Dynamics Research

Dave Reedy
Material Mechanics

Martin Heinstein
Computational Solid Mechanics and Structural Dynamics

Maarten de Boer
MEMS Technology

Jim Knapp
Radiation Solid Interactions and Processing

Ed Piekos and Channy Wong
Microscale Science and Technology

Liz Holm
Materials and Process Modeling

Sandia National Laboratories
P.O. Box 5800
Albuquerque, NM 87185-0847

Abstract

The Microsystems Subgrid Physics project is intended to address gaps between developing high-performance modeling and simulation capabilities and microdomain specific physics. The initial effort has focused on incorporating electrostatic excitations, adhesive surface interactions, and scale dependent material and thermal properties into existing modeling capabilities. Developments related to each of these efforts are summarized, and sample applications are presented. While detailed models of the relevant physics are still being developed, a general modeling framework is emerging that can be extended to incorporate evolving material and surface interaction modules.

Acknowledgments

Specific contributions of many individuals are noted at the end of the relevant sections. In addition, the authors are especially appreciative of the efforts of Michail Gallis and O. Burak Ozdoganlar who provided thoughtful technical reviews of the entire report.

Contents

1.0 Introduction 9
2.0 Electrostatic Loading of Microstructures 11
2.1 Introduction 11
2.2 Electrostatic Pressure Loading 11
2.3 Adagio Electrostatic Pressure Subroutine 12
2.4 Axial Bar Test Problem 13
2.5 μbeam Deflection Illustration 14
2.6 Summary 14
2.7 Acknowledgements 14
2.8 References 15
3.0 Simulation of Surface Interactions 17
3.1 Introduction 17
3.2 The Cohesive Zone Model for Crack Propagation 17
3.3 Adaptation of Cohesive Zone Model to Adhesion Simulations 18
3.4 TAHOE Simulation of a SMM Cantilever Beam Adhesion Test Structure 19
3.5 JAS3D's Implementation of a Cohesive Zone Model 19
3.6 JAS3D's Simulation of a Peel Test 21
3.7 Plans for Future Developments 21
3.8 References 21
4.0 Effect of Nanotexturing on Interfacial Adhesion in MEMS 28
4.1 Introduction 28
4.2 Sample Preparation 28
4.3 Adhesion Test Results 29
4.4 Analysis 30
4.5 Discussion 31
4.6 Summary and Conclusions 33
4.7 Acknowledgements 33
4.8 References 33
5.0 Noncontinuum Thermal Transport 35
5.1 Introduction 35
5.2 Objectives 35
5.3 Summary of Progress 36
5.3.1 Macroscale Tool Modification 36
5.3.2 Microscale Tool Development 38
5.4 Plans for Future Developments 40
5.4.1 Macroscale Tool Modification 40
5.4.2 Microscale Tool Development 40
5.5 References 40
6.0 Network Algorithms for Minimum Energy Fracture Surfaces 42
6.1 Introduction 42
6.2 Fracture Model 42
6.3 Equiaxed Polycrystals 44
6.4 Microcracked Polycrystals 45
6.5 Conclusions 46
6.6 Future Work 47

6.7 References 48

Figures

2.1 Electrostatically deformed spring problem used to illustrate the pull-in instability. 16
2.2 Adagio regression test problem with aluminum bar loaded axially using electrostatic pressure. 16
2.3 Bar tip deflection resulting from electrostatic excitation, illustrating nonlinear response to increasing voltage and instability point. 16
2.4 Beam bending problems demonstrating distributed electrostatic pressure load. 16
2.5 Adagio computed beam deflections resulting from full-span electrostatic excitation in comparison to reference deflections from Abaqus. 16
3.1 Cohesive zone model for interfacial separation with behavior in the cohesive zone defined by traction-separation relation. 23
3.2 Finite element model of a surface micromachined cantilever beam adhesion test structure by de Boer and Michalske. 23
3.3 Normal traction depends only on normal separation in the simplified version of the Xu-Needleman model used in adhesion test structure simulation. 24
3.4 Calculated nonadhered length vs. support post height of a surface micromachined cantilever beam adhesion test structure. 24
3.5 Calculated cohesive zone length vs. the characteristic separation distance. 25
3.6 Mesh used in the MEMS peel simulation. 25
3.7 The effective relationship used in the MEMS peel simulation. 26
3.8 Deformation of peeled strip. 26
3.9 Calculated crack length vs. end displacement for baseline and refined mesh. 27
4.1 (a) ground plane polysilicon (poly 0) oxidation (b) cantilever fabrication, (c) release and coating (d) testing. 28
4.2 Polysilicon ground plane surface textures versus oxidation times. 29
4.3 Experimental and calculated results for adhesion versus average roughness. 30
4.4 Calculated relative contributions to the adhesion versus gap at each location. 32
5.1 Schematic picture of the product emulator. 36
5.2 Predicted temperature profile of the optical shutter using the bulk silicon thermal conductivity. 37
5.3 Predicted temperature profile of the optical shutter using the undoped polysilicon thermal conductivity. 38
5.4 Demonstration of (a) diffusive-dominated and (b) ballistic-dominated heat transport following a short-duration energy input at the domain center. 39
6.1 Grain structures represented by networks 44
6.2 Intergranular fracture surfaces of minimum surface formation energy for equiaxed polycrystals with uniform boundary strength. 44
6.3 Minimum surface formation energy intergranular fracture surface size as a function of equiaxed grain size in 2D and 3D 45
6.4 Intergranular fracture surface of minimum surface formation energy for equiaxed polycrystals. 46
6.5 Normalized intergranular fracture surface size as a function of fraction microcracked boundaries in 2D and 3d. 47

Tables

4.1 Polysilicon versus oxidation time roughness. 29
4.2 Microsystem applications of network optimization algorithms 47

This page intentionally blank

1.0 INTRODUCTION

The successful migration of microelectromechanical systems (MEMS) components from the laboratory to the stockpile requires the development of high fidelity modeling capabilities to ensure adequate performance after many years of dormancy. Because of the high surface area to volume ratio of surface micro-machined devices, adhesion, friction, and wear have been identified as key technological barriers to their implementation in weapons. Furthermore, some material properties exhibit a scale dependence, which, under some conditions, may dramatically affect device performance and reliability.

To begin to address these many needs, the ASCI Microsystems Subgrid Physics project was initiated with a charter to establish a modeling infrastructure that accurately treats microscale material mechanics and surface interactions. This capability will enable accurate assessment of MEMS performance prior to fabrication as needed to support component design. The three primary objectives of this program are:

- Development of a coupled electromechanical modeling capability for analyzing electrostatically deformed MEMS devices.
- Development of surface interaction laws appropriate for MEMS devices, initially focusing on the surface adhesion phenomenon.
- Development of scale dependent thermal and material mechanics models.

While a variety of actuation schemes for driving micro-components have been demonstrated, a vast majority of devices have relied on electrostatic attraction as the prime mover. The interaction between electric field and structural deformations poses a challenging modeling problem that, in its general form, requires a two-way coupling of electric field and mechanical deformation solvers. From the mechanical perspective, the electrostatic field generates nonuniform surface pressures that vary nonlinearly with structural deformations. Consequently, necessary modifications for handling nonuniform surface pressures were incorporated into the nonlinear quasistatic finite element code Adagio being developed in the SIERRA architecture. As described in section 2, this framework enables the insertion of distributed surface pressures produced by an external electrostatic field solver. The near term absence of such a code in SIERRA, however, prompted the further development of a nonlinear deformation dependent electrostatic loading routine in Adagio, based on a parallel plate capacitance model. These routines are now an integral part of the Adagio code and are useful for providing design support for a large class of microsystems.

Adhesion is a complex phenomenon exhibited by two surfaces brought into close proximity. One approach for including surface interactions in a finite element code is to adapt the cohesive zone model, normally used to simulate material separation, to adhesion. The cohesive zone model is usually implemented as a surface element, but in the present study it has been implemented in the JAS3D production code as a contact condition as summarized in Section 3. This type of implementation was chosen since it appears is more easily adapted to adhesional interactions between initially separated, 3D bodies. Furthermore a contact-based approach can be incorporated in SIERRA using the ACME contact architecture.

A sub-grid exploration of the effect of surface texture on adhesion in MEMS devices is presented in Section 4, illustrating the significant contributions of noncontacting surface features to the total adhesion energy. Spanning the scale from these subgrid adhesion models to grid scale traction separation laws will be the focus of future modeling efforts.

Section 5 summarizes the results of an investigation into the scale dependency of polysilicon thermal properties. Of special interest is the response of components under an abnormal environment, such as fire, as well as thermal management of components in proximity of energy sources, such as a VCSEL. The microstructures are made of multiple heterogeneous layers (thin-film) of materials with very small film thickness. For studying thermal responses of such a small structure, it is important to recognize that the cross-plane and in-plane heat conduction coefficients can be different than the bulk coefficient. In addition, the possible influence of ill-defined surface contacts is considered as well.

Finally, three-dimensional fracture of polysilicon surfaces is examined in Section 6 through application of network optimization algorithms. The minimum expended energy for fracture is the free energy required to form two new surfaces. For intergranular fracture, the minimum surface formation energy is complicated by the rough fracture surface, with area greater than the specimen cross-section. We utilize network optimization algorithms to determine the minimum surface formation energies and surfaces in two- and three-dimensional polycrystals. For equiaxed grains and uniform boundary strength, the minimum energy fracture area is independent of grain size and is larger than the specimen cross-section. In systems with microcracked boundaries, the fracture surface deviates to include microcracked boundaries, creating interlocking grain configurations, and a unique fracture percolation threshold is observed. Further applications of network optimization algorithms are discussed.

2.0 ELECTROSTATIC LOADING OF MICROSTUCTURES

2.1 INTRODUCTION

Although a variety of actuation methods have been proposed for microsystems, including thermal deformation (Ref. 2.1), shape memory alloys (Ref. 2.2), and magnetic attraction (Ref. 2.3), the vast majority of devices developed to date have relied on electrostatic forces. The comb drive, for example, efficiently converts electrical energy to linear motion, and has therefore become the actuation standard in the microsystem design library (Ref. 2.4). The complicated electrical field present at the comb drive tips requires a truly coupled electromechanical simulation to predict performance and enable design optimization (Ref. 2.5). Commercial codes such as CoventorWare (Ref. 2.6) have been developed to treat these problems using a weak coupling between mechanical and electrical field solvers, but these codes are generally only available for serial computations and are therefore limited to relatively simple designs.

A large class of systems, however, relies on a simpler mode of operation whereby a compliant structure is attracted to a rigid substrate. Optical switches (Ref. 2.7), a friction test structure (Ref. 2.8) and an inchworm actuator (Ref. 2.9) are recent examples of such devices for which the actuation force can be adequately described using a nonlinear parallel plate capacitance model. Such models have been implemented in Abaqus (Ref. 2.10) and used successfully, but the growing need for modeling and simulation of increasingly complex microsystems warrants an increased emphasis on applying Sandia's high performance computing capability to these problems.

As an initial step toward meeting this need, a nonuniform deformation-dependent pressure loading routine has been developed in the nonlinear quasi-static analysis code Adagio (Ref. 2.11) to mimic electrostatic forces. The nonlinear loading depends strongly on the structural deformations, and can lead to the well-known electrostatic instability (Ref. 2.12). Recent addition of the tangent stiffness solution algorithm to the Adagio suite enables simulation of planar MEMS devices. This memorandum summarizes the electrostatic pressure loading routine and its implementation. A test problem featuring an axially loaded bar that was developed for inclusion in the Adagio regression test suite is first summarized, followed by two examples of beams loaded to the brink of instability.

2.2 ELECTROSTATIC PRESSURE LOADING

The attractive force between two parallel plate conductors separated by a dielectric is given by (Ref. 2.13)

$$F(g,V) = \frac{1}{2}\frac{\varepsilon A V^2}{g^2}, \tag{2.1}$$

in which ε is the permittivity of the dielectric, A is the area of the plate, V is the potential difference, and g is the separation distance. To illustrate the character of electrostatic loading, consider the spring balance problem shown in Figure 2.1. The potential difference across the gap stretches the linear spring k which in turn closes the gap,

altering the electrostatic force. The relationship between the applied field and the static spring deformation is defined by the force balance

$$k\delta = \frac{1}{2}\frac{\varepsilon A V^2}{(g_o - \delta)^2}. \tag{2.2}$$

Rearranging, the equilibrium deformation is given by the roots of the cubic equation

$$\delta^3 - 2g_o\delta^2 + g_o^2\delta = \frac{\varepsilon A}{2k}V^2, \tag{2.3}$$

which for low voltage has one physically realistic root. As V is increased, the deflection increases at an increasing rate until electrostatic instability is attained. This critical point can be found by solving $dV/d\delta=0$, leading to the critical deflection

$$\delta^* = \frac{1}{3}g_o \tag{2.4}$$

and the critical excitation

$$V^* = \sqrt{\frac{8}{27}\frac{k}{\varepsilon A}g_o^3}. \tag{2.5}$$

While it's possible to exceed the critical voltage in a dynamic environment as needed to maximize deflections in some devices (Ref. 2.14), static excitation beyond the critical voltage would cause a sudden gap closure. This may be useful in designing a switch, but it can also represent failure in some microactuators.

In many microsystems, polysilicon beam and plate structures are deformed using a potential difference between the structure and a conductive layer bonded to the relatively rigid substrate. As the structure deforms, the local gap distance changes leading to nonuniformity of the applied force. For a structure defined in the x-y plane, a distributed pressure loading can be defined based on the local deformation according to

$$p(x,y,V) = -\frac{1}{2}\frac{\varepsilon V^2}{(g_o - z(x,y))^2}, \tag{2.6}$$

where the out of plane deflection is defined by $z(x,y)$. Casting the loading in this form preserves the character of the electrostatic force, including the important potential for electromechanical instability. Unfortunately, the critical voltage cannot easily be determined analytically for the general structure, so finite element modeling in the design phase followed by careful experimentation with the finished device are needed to establish safe operating boundaries.

2.3 ADAGIO ELECTROSTATIC PRESSURE SUBROUTINE

Implementation of electrostatic pressures in Adagio was accomplished through modification of the uniform external pressure loading routine, Adagio_Fext_Pressure_ug3dq4_Support.C. Modifications were made to include electrostatic specific input variables, nonuniform loading, and computation of the local

nonlinear deformation dependent pressure. These modifications form the basis of the new electrostatic pressure loading routine Adagio_Fext_ESPress_ug3dq4_Support.C that can be accessed using the boundary condition call:

Electrostatic pressure with ground <<location>> with permittivity <<value>> using function <<votage definition>> scaled by <<factor>>.

In its current form, the routine can be used to compute electrostatic pressures on planar x-y surfaces deflecting in the z direction. The reference ground plane is defined by a single global z coordinate using units consistent with the mesh. Similarly, the permittivity and the voltage time history must be entered using consistent coordinates. The scale factor offers an effective way of changing the direction of the loading relative to the surface normal by entering +/-1.

Accommodating the nonuniform surface pressure required modification of the scalar pressure variable to a vector of length equal to the number of faces in the sideset. At each time step, the center coordinates for each face are computed by averaging the corner node locations, and the z coordinate is used to determine the local gap relative to the ground plane location. The resulting face pressure is then computed using the current voltage value, and then decomposed into nodal forces used to update the deformation. The Adagio solver iterates on these calculations to achieve static equilibrium as defined by a user specified tolerance. The vector representation of the pressure distribution is an important feature of this development regardless of the source of the electrostatic load calculation. Future high fidelity simulations featuring full 3D field solvers can be coupled to the Adagio code using this data structure.

2.4 AXIAL BAR TEST PROBLEM

The basic functionality of the subroutine can be illustrated by an axially loaded bar shown in Figure 2.2. While this problem is not very practical from a microsystems perspective, it is a version of the spring balance problem ($k=EA/L$) whose closed form solution makes it a useful part of the Adagio regression test suite. The 1"x0.1"x0.1" aluminum bar ($E=10x10^6$ *psi*) is modeled using 10 hex elements along its length. An electrostatic load is applied to the end of the aluminum bar across an air gap ($\varepsilon=2x10^{-12}$ lb/V^2, $g_o=40\mu in$), causing the bar to stretch. The gap in turn narrows, leading to an increase in the applied load. Note that the voltage-deflection relationship for this problem is independent of the beam cross-sectional area since both the beam stiffness and the net axial load depend linearly on this paramater.

The gap influence is illustrated by the nonlinear tip deflection response shown in Figure 2.3. The deflection increases until the critical voltage is reached ($V=308V$), at which point the tip deflection is equal to 1/3 the initial gap distance. Beyond this point, the closed-loop system stiffness becomes negative and no realistic solution exists. In practice, the bar would instantaneously snap down to the substrate. The Adagio solution accurately depicts the exact solution to within numerical accuracy up to the point of instability. This problem has been added to the Adagio regression test suite and can be found under the name ‘bar_espress’.

2.5 μBEAM DEFLECTION ILLUSTRATION

To illustrate the electrostatic loading on problems of MEMS significance, we consider a polysilicon (E=160GPa) beam of dimension 200μm long, 20 μm wide, and 2μm thick. The beam is modeled using a 40x4 mesh of shell elements and the electrostatic loading is applied along the entire span as shown in Figure 2.4. Two sets of boundary conditions representing idealizations of existing MEMS devices were chosen: a cantilever beam with initial gap of 6 μm, and a double-cantilever (axial slip allowed) with an initial gap of 3μm.

The beam tip (cantilever) and midspan (double-cantilever) deflections are shown in Figure 2.5. In the absence of closed form solutions for these problems, the Adagio results are shown in comparison to the results obtained using a 200-element beam model in Abaqus (Ref. 2.10). The two deflections compare to within 0.2% up to the electrostatic instability points, predicted by Abaqus to be 74 and 169 volts for the cantilever and double cantilever beams, respectively.

2.6 SUMMARY

The gradual progression of microsystems from the laboratory to the stockpile requires a commensurate development of modeling and simulation capabilities needed for design optimization and qualification. As a consequence of their small size and high surface area to volume ratio, electrostatic forces have proven to be an effective method for actuating microdevices, and the majority of micro-actuators developed to date have been based on this coupled phenomenon.

In the absence of a truly coupled electromechanical modeling capability, a parallel plate capacitance load suitable for modeling a large class of actuators has been implemented in Adagio. The routine computes a nonuniform pressure distribution on the actuation surface based on the nodal deflections and the voltage across the gap. The subroutine was tested on a model of an axially loaded bar and compared favorably to the exact solution. Beam problems that are representative of existing MEMS actuation devices were also simulated and compared to solutions obtained with Abaqus. Results verify the proper implementation of the subroutine, enabling its use for large-scale simulation of many electrostatically deformed microdevices.

Future work will focus on developing more robust three-dimensional representations of the electric field and its resulting pressure, as well as other coupled physics (such as gas damping) effects that strongly affect the dynamic response of microdevices. The new capability added to Adagio to enable nonuniform surface pressure provides a foundation for accommodating these effects.

2.7 ACKNOWLEDGEMENTS

John Mitchell provided valuable guidance for developing the deformation dependent pressure distribution in Adagio, and Ken Alvin assisted with the use of the tangent-stiffness pre-conditioner that enabled solution of the beam deformations.

2.8 REFERENCES

2.1 Ohmichi, O., and Yamagata, Y., "Micro Impact Drive Mechanisms Using Optically Excited Thermal Expansion," *Journal of Microelectromechanical Systems*, Vol. 6. No. 3, September 1997, pp. 200-207.

2.2 Gill, J.J, and Carman, G.P., "Thin Film NiTi Shape Memory Alloy Microactuator with Two-Way Effect," *Proceedings of the 2000 ASME International Mechanical Engineering Congress and Exposition*, November 2000, MEMS Vol. 2, pp. 89-95.

2.3 Judy, J.W., and Muller, R.S., "Magnetic Microactuation of Polysilicon Flexure Structures," *Journal of Microelectromechanical Systems*, Vol. 4. No. 4, December 1995, pp. 162-169.

2.4 Garcia, E.J. and Siegowski, J.J., "Surface Micromachined Microengine as the Driver for Micromechanical Gears," *Proceedings of the Transducers '95 - Eurosensors IX*, June 25-29, 1995, Stockholm, Sweden.

2.5 Johnson, W.A., and Warne, L.K., "Electrophysics of Micromechanical Comb Actuators," *Journal of Microelectromechanical Systems*, Vol. 4, No.1, March 1995, pp. 49-59.

2.6 CoventorWare, http://www.coventor.com/software/coventorware/index.html.

2.7 Bishop, D.J., Giles, R.G. and Das, S.R., "The Rise of Optical Switching," Scientific American, January 2001, pp. 88-94.

2.8 de Boer, M.P., Redmond, J.M., and Michalske, T.A., "A Hinged-Pad Test Structure for Sliding Friction Measurement in Micromachines," *Proceedings of the SPIE Conference on Materials and Device Characterization in Micromachining*, Santa Clara, CA, 1998, Vol. 3512, pp. 241-251.

2.9 de Boer, M.P., Luck, D.L., Walraven, J., and Redmond, J.M., "Characterization of an Inchworm Actuator Fabricated by Polysilicon Surface Micromachining," Proceedings of the 2001 SPIE Symposium on Micromachining and Microfabrication, San Francisco, CA, October 21-24, 2001.

2.10 Hibbitt, Karlsson, & Sorensen, Inc, 1998, *Abaqus Standard/User's Manual*, version 5.8.

2.11 Mitchell, J.A., Gullerud, A.S., Scherzinger, W.N., Koteras, R., and Porter, V.L., "Adagio: Nonlinear Quasistatic Structural Response Using the SIERRA Framework," *First MIT Conference on Computational Fluid and Solid Mechanics*, Elsevier Science 2001.

2.12 Osterberg, P.M., Gupta, R.K., Gilbert, J.R., and Senturia, S., "Quantitative Models for the Measurement of Residual Stress, Poisson Ratio, and Young's Modulus Using Electrostatic Pull-in of Beams and Diaphragms," *Proceedings of the Solid-State Sensor and Actuator Workshop*, Hilton Head, South Carolina, June 13-16, 1994, pp. 184-188.

2.13 Senturia, S.D., *Microsystem Design*, Kluwer Academic Publishers, Boston, MA, 2000, pp. 130-137.

2.14 Redmond, J.M., de Boer, M.P., and Michalske, T.A., "Integrated Modeling and Testing of a Micro Hinged Structure for Sliding Friction Measurement," *Proceedings of the 1998 ASME International Mechanical Engineering Congress and Exposition*, Anaheim, CA, November 1998.

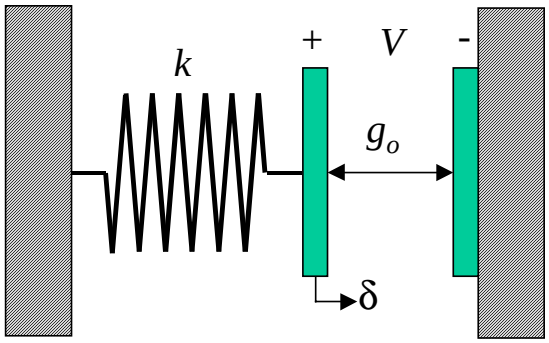

Figure 2.1. - Electrostatically deformed spring used to illustrate the pull-in instability.

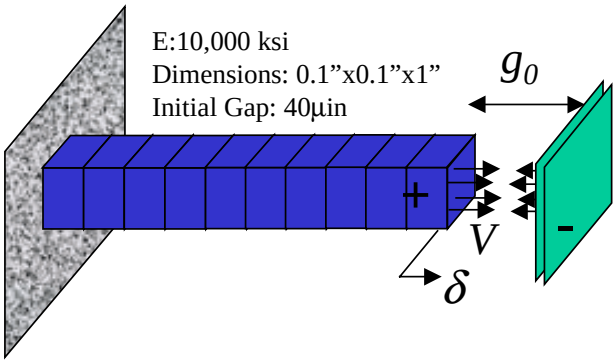

Figure 2.2. - Regression test problem with aluminum bar loaded axially with electrostatic pressure.

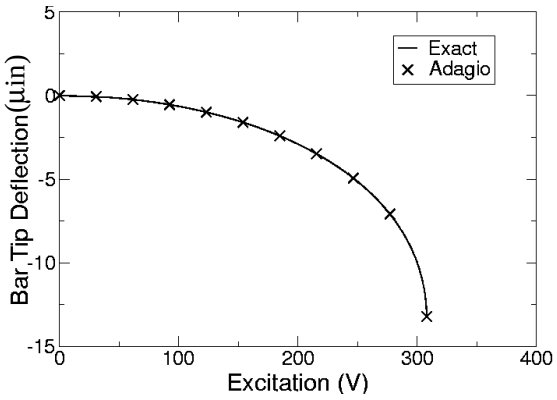

Figure 2.3. - Bar tip deflection resulting from electrostatic excitation, illustrating nonlinear response to increasing voltage and instability point.

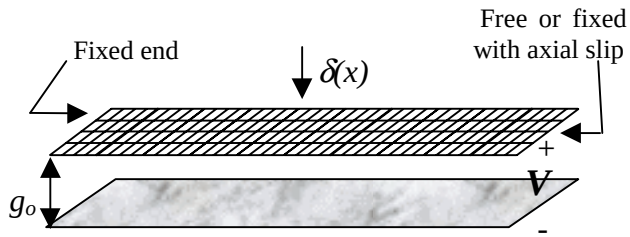

E: 160 Gpa
Dimensions: 200x20x2 µm
Initial Gap: 6 µm (Free), 3µm (Fixed)

Figure 2.4. – Beam bending problems demonstrating distributed electrostatic pressure load.

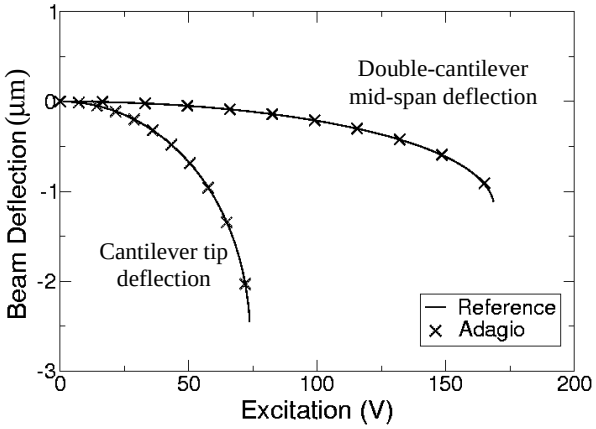

Figure 2.5. - Adagio computed beam deflections resulting from full span electrostatic excitation in comparison to reference.

3.0 SIMULATION OF SURFACE INTERACTIONS

3.1 INTRODUCTION

The high surface area to volume ratio of MEMS components accentuates the effect of adhesional and frictional forces on performance and reliability. Thus, accurate surface interaction models must be incorporated in the finite element codes used to simulate MEMS performance. It is desirable that the surface interaction models governing adhesion and frictional forces be 1) as simple as possible while still capturing the essence of the surface interactions, 2) defined in terms of physically-based parameters, 3) readily implemented in a finite element code, and 4) consistent with a characteristic element size of on the order of a micron (i.e., on the scale of MEMS structures, not on the scale of atoms). An approach that adapts the widely used cohesive zone model for simulating interfacial crack propagation to the modeling of adhesional effects appears to best meet the stated criteria.

The following will discuss progress towards the development and implementation of adhesional models in SNL finite element codes. First, the cohesive zone model, as applied to crack propagation, is briefly reviewed. This is followed by a discussion of how the cohesive zone model can be adapted to simulate adhesional effects. Several illustrative results are then presented for a surface micromachined, cantilever beam adhesion test structure. These initial results were obtained using Sandia's Tahoe finite element code. Tahoe implements the cohesive zone model via surface-like finite elements, an approach that does not appear easily adaptable to the general case of 3D bodies that are initially separated by relatively large distances (the connecting surface elements are difficult to define). The cohesive zone model can also be implemented as a contact condition, and this type of implementation does appear to be more readily extended to adhesional interactions between initially separated, 3D bodies. A contact condition-based cohesive zone model has been implemented in Sandia's JAS3D finite element code to investigate the merits of this approach. JAS3D's cohesive zone model is described and results of a peel test simulation are presented. This progress report concludes with suggestions for future work.

3.2 THE COHESIVE ZONE MODEL FOR CRACK PROPAGATION

In recent years many members of the fracture community have adopted a cohesive zone model (Ref. 3.1-3.2), based upon traction-separation (σ–δ) relations, to simulate crack propagation (Ref. 3.3-3.10). Separation is modeled as a gradual process that takes place across an extended crack tip, with tractions resisting the separation in the cohesive zone (Figure 3.1). The σ–δ relation can be thought of as a phenomenological characterization of the rupture processes occurring in the crack-tip fracture process zone. The two key parameters defining a σ–δ relation are the peak separation stress $\hat{\sigma}$ and the work of separation (the area under the σ–δ curve). The exact shape of the curve seems to be of secondary importance, although the critical distance δ_c, where the resisting tractions vanish, does directly influence the length of the cohesive zone. Note that the actual length of the cohesive zone can vary as the crack grows, and must be determined as part of the solution.

The σ–δ approach appears particularly promising for several reasons. It 1) is intuitively appealing to characterize interfacial separation by a traction–separation relationship, 2) is computationally attractive since crack growth is a natural outcome of the solution, and 3) reduces to classical linear elastic fracture mechanics when elastic materials are subjected to a pure Mode I or Mode II loading. Moreover, this type of approach can potentially lead to mesh-independent results since a length scale is embedded within the σ–δ relationship (i.e., stress vs. displacement, not stress vs. strain). This approach is particularly well suited for simulating interfacial fracture since the crack path is predefined. Note that a necessary condition for a converged solution is that the tractions in the cohesive zone must be resolved by the spatial discretization. Therefore, mesh size along the potential crack path has to be chosen in a way that is consistent with the σ–δ relation. The main drawback in using a cohesive zone modeling approach for simulating interfacial fracture is uncertainty in how to choose the material parameters defining the σ–δ relationship. At the present time interfacial σ–δ relations are chosen in an ad hoc manner by matching available fracture test data. There is yet no rigorous theory for measuring and defining a unique σ–δ relationship for a given material interface.

3.3 ADAPTATION OF COHESIVE ZONE MODEL TO ADHESION SIMULATIONS

When the traction-separation relation used in a cohesive zone model is derived from a potential, as is typically the case, and when all materials are elastic, the solution is path independent. A crack grows when joined bodies are pulled apart, but the crack heals and returns to its initial length when the load is reversed. The σ–δ relationship can be thought of as defining the adhesional force that must be overcome during separation. When using a cohesive zone model for simulating crack propagation, the potential function typically defines both normal and tangential stresses and there is in general a mixed-mode crack-tip deformation state. In contrast, adhesional forces are usually associated with only normal stress and consequently, the potential function should be defined (or specialized) to depend only on normal separation. Constraints against interpenetration can be directly enforced, or alternately the σ–δ relationship can be defined to include a repulsive force.

Although cohesive zone models used for simulating the separation of bonded materials are conceptually similar to those used to simulate the attraction of neighboring materials, there can be significant differences in implementation. For example, a small displacement formulation is generally appropriate for modeling crack propagation since the bonded materials are initially in contact and rupture occurs at relatively small displacement (relative to element size). On the other hand, a large displacement formulation may be needed for adhesion problems since the initial gap may be large relative to the elements. Widely separated bodies may move toward each other and then be drawn together by adhesional forces. Furthermore, frictional forces can be generated when adhered bodies are in contact and subjected to normal compression. Such frictional forces are not determined via the potential function, but are determined by contact stress and relative tangential displacement. This is in contrast to bonded materials where the potential function usually defines the resistance to relative tangential displacement.

3.4 TAHOE SIMULATION OF A SURFACE MICROMACHINED, CANTILEVER BEAM ADHESION TEST STRUCTURE

In the early phase of this work, the Tahoe finite element code (http://tahoe.ca.sandia.gov/html/docs.html) was used to simulate the surface micromachined, cantilever beam adhesion test structure used by de Boer and Michalske (Ref. 3.11). Figure 3.2 defines the test structure analyzed, while Figure 3.3 shows the σ–δ relationship used in the calculations. This σ–δ relationship is a simplified version of the relationship used by Xu and Needleman (Ref. 3.10) specialized so that normal traction depends only on normal separation and no tangential traction is generated. This σ–δ relationship depends only on the work of normal separation G_o (an experimentally measured value of 11.3 mJ/m^2 is used in the calculations) and the characteristic separation distance δ^* (defined as the δ value at peak traction). In the experiment, a long, slender silicon beam is supported at one end and cantilevered over a silicon substrate. Adhesional forces pull the unsupported end of the beam into contact with the substrate, and the adhesional forces cause long beams to be adhered over a large fraction of their length. A beam theory-based solution can be used to predict the nonadhered length s as a function of the height of the support post h (Figure 3.2). Figure 3.4 shows that this analytic solution is in excellent agreement with finite element results (δ^*=10 nm). Results for two different element size (D=1.0 and 0.5 micron) show the results are mesh-independent. This is as expected since the calculated 11-micron length of the cohesive (adhesive) zone is fully resolved by a 1-micron element length. Similar calculations show that the calculated relationship between nonadhered length and the height of the support post is 1) insensitive to the details of the shape of the σ–δ relationship and 2) insensitive to the value of the characteristic separation distance when δ^* is between 1 and 10 nm (the length of the cohesive zone does vary with δ^*). Interestingly, the extreme compliance of the slender silicon beam generates cohesive zone lengths that are orders of magnitude longer than the characteristic separation distance (Figure 3.5). This result indicates that a relatively coarse finite element mesh can be used; the characteristic element length can be 3 orders of magnitude larger than δ^*.

Note that in these quasi-static simulations, the beam and substrate were initially adhered along their length, and the model was loaded by displacing the substrate downward while fixing the left-hand side of the beam. These were actually interfacial crack growth simulations. Convergence problems frustrated attempts to start with an initially separated beam and substrate and then push the free end of the beam towards the substrate. A long length of the beam tried to jump into contact as soon as the beam's free end came into contact. As might be expected, snap-buckling-like response proved difficult to simulate in a quasi-static calculation. Dynamic simulations, especially those using an explicit solver, should be more successful.

3.5 JAS3D'S IMPLEMENTATION OF A COHESIVE ZONE MODEL

There are several different ways of implementing σ–δ relations in a finite element setting: as a mixed boundary condition, as a contact surface condition, or as constitutive relations in a surface-like finite element (the approach used in Tahoe). As noted above, it may prove difficult to adapt an implementation based upon surface-like finite elements to

the general case of initially separated 3D bodies (the connecting surface elements are difficult to define). It appears that this potential limitation can be avoided when the σ–δ relations are implemented as a contact surface condition. A contact condition-based cohesive zone model has been implemented in Sandia's JAS3D finite element code to investigate the merits of this approach. This implementation is an extension of ideas initially developed for the Point Weld Friction Model (see the JAS3D manual, http://sass2248.jal.sandia.gov/SEACAS/Documentation/JAS3D.pdf).

The σ–δ relations implemented in JAS3D are the same as those used by Tvergaard and Hutchinson (they call their model the Embedded Process Zone (EPZ) model (Ref. 3.9)). They define a cohesive potential that depends on a scalar, effective separation. The effective separation λ is expressed in terms of the normal (δ_n) and tangential (δ_t) components of the displacement difference of initially coincident points on the interface

$$\lambda = \sqrt{\left(\frac{\delta_n}{\delta_n^c}\right)^2 + \left(\frac{\delta_t}{\delta_t^c}\right)^2} \quad . \tag{3.1}$$

The parameters δ_n^c and δ_t^c are critical values of these displacement components, and are defined so that when λ=1, the tractions drops to zero. The function σ(λ) is the effective traction vs. separation relationship, and is used to define a traction potential,

$$\phi(\delta_n, \delta_t) = \delta_n^c \int_0^\lambda \sigma(\lambda')d\lambda' \tag{3.2}$$

Consequently, the normal and tangential traction components that act across the interfacial cohesive zone are

$$T_n = \frac{\partial \phi}{\partial \delta_n} = \frac{\sigma(\lambda)}{\lambda}\frac{\delta_n}{\delta_n^c} \quad \text{and} \quad T_t = \frac{\partial \phi}{\partial \delta_t} = \frac{\sigma(\lambda)}{\lambda}\frac{\delta_n^c}{\delta_t^c}\frac{\delta_t}{\delta_t^c} \tag{3.3}$$

The relative contribution of shear and normal displacement (i.e., for a mixed-mode loading) is determined by specifying the value of the ratio δ_n^c/δ_t^c. Under a pure normal separation ($\delta_t = 0$), $T_n = \sigma(\lambda)$ with $\lambda = \delta_n/\delta_n^c$ and with a peak normal traction of $\hat{\sigma}$ (Figure 3.1). Under a pure tangential displacement ($\delta_n = 0$), $T_t = (\delta_n^c/\delta_t^c)\sigma(\lambda)$ with $\lambda = \delta_t/\delta_t^c$ and with a peak tangential traction of $(\delta_n^c/\delta_t^c)\hat{\sigma}$. Note that by choosing $\delta_t^c >> \delta_n^c$, T_t can be made vanishingly small, and only a normal traction is generated.

The work of separation per unit area of interface is path independent and equals the value of the potential ϕ (Eq. 3.2) evaluated at λ = 1. Note that the formulation allows reversible behavior prior to attaining λ = 1. In the JAS3D implementation, the connection implied by σ–δ relationship is permanently broken once λ>1. If the separated surfaces should subsequently come into contact, the contact algorithm then governs their interactions. Also note that the JAS3D implementation constrains interfacial normal separation to prevent interpenetration when λ<1.

The Cohesive Zone model is one of JAS3D's friction models. The interface where the cohesive zone forms is defined by a node set that interacts with a master surface/material. The parameters defining the COHESIVE ZONE model are:

1) Critical normal gap, δ_n^c
2) Critical tangential gap, δ_t^c
3) σ–δ function, $\sigma(\lambda)$ (defined using the Function command)
4) Parent surface/material of the Cohesive Zone model's node set (to define contact interactions once λ>1)

3.6 JAS3D'S SIMULATION OF A PEEL TEST

JAS3D has been used to simulate the peeling of a silicon beam off of a rigid substrate. The silicon beam is 100 μm long by 2.3 μm high by 1 μm deep. Calculations were carried out with both a baseline and a refined mesh. The baseline mesh is 100 elements long (i.e., 1 μm long elements) and is 2 elements high (Figure 3.6). The refined mesh is 200 elements long (i.e., 0.5 μm long elements) and is 4 elements high. Figure 3.7 shows the $\sigma(\lambda)$ that was used ($\delta_n^c = \delta_t^c$ = 5x10^{-5} mm, $\hat{\sigma}$ = 0.452 MPa, and the separation energy --to overcome adhesional forces—equals 11.3 mJ/m^2). As the beam end is pulled off the substrate, the loaded end is free to rotate and the detached length steadily increases (Figure 3.8). The cohesive zone quickly attains a steady state length of 13 μm. Since the baseline mesh has an element length of 1 μm, the cohesive zone is fully resolved by the mesh (cohesive zone is 13 elements long). Figure 3.9 plots detached length vs. end displacement for the baseline and the refined mesh. As expected, the results are mesh-size independent. Note that JAS3D has difficulty with thin, beam-like structures, and this foiled attempts to simulate the surface micromachined, cantilever beam adhesion test structure (Figure 3.2).

3.7 PLANS FOR FUTURE DEVELOPMENTS

The work reported here represents an initial effort towards implementing surface interaction models in SNL finite element codes for analyzing MEMS components. Continuing and planned work includes:

1. Extending the contact condition-based cohesive zone model in JAS3D to a large displacement formulation, as needed in general, 3D MEMS simulations.
2. Implementing the contact condition-based cohesive zone model in an explicit dynamics finite element code so that unstable, snap-buckling-like response can be simulated.
3. Implementing improved adhesion and friction MEMS surface interaction models as they become available.

3.8 REFERENCES

3.1 Barrenblatt, G.I., *The mathematical theory of equilibrium of cracks in brittle fracture.* Advances in Applied Mechanics, 1962. **7**: p. 55-129.

3.2 Dugdale, D.S., *Yielding of steel sheets containing slits.* Journal of the Mechanics and Physics of Solids, 1960. **8**: p. 100-104.

3.3 Camacho, G.T. and M. Ortiz, *Computational Modelling of Impact Damage in Brittle Materials.* International Journal of Solids and Structures, 1996. **33**: p. 2899-2938.

3.4 Geubelle, P.H. and J.S. Baylor, *Impact-induced delamination of composites: a 2D simulation.* Composites Part B, 1998. **29B**: p. 589-602.

3.5 Needleman, A., *An analysis of tensile decohesion along an interface.* Journal of the Mechanics and Physics of Solids, 1990. **38**: p. 289-324.
3.6 Ortiz, M. and A. Pandolfi, *Finite-Deformation Irreversible Cohesive Elements for Three-Dimensional Crack-Propagation Analysis.* International Journal for Numerical Methods in Engineering, 1999. **44**: p. 1267-1282.
3.7 Rahul-Kumar, P., et al., *Polymer interfacial fracture simulations using cohesive elements.* Acta Materialia, 1999. **47**: p. 4161-4169.
3.8 Reedy, E.D., Jr., F.J. Mello, and T.R. Guess, *Modeling the Initiation and Growth of Delaminations in Composite Structures.* Journal of Composite Materials, 1997. **31**: p. 812-831.
3.9 Tvergaard, V. and J.W. Hutchinson, *The influence of plasticity on mixed mode interface toughness.* Journal of the Mechanics and Physics of Solids, 1993. **41**: p. 1119-1135.
3.10 Xu, X.-P. and A. Needleman, *Numerical simulations of dynamic crack growth along an interface.* International Journal of Fracture, 1996. **74**: p. 289-324.
3.11 de Boer, M.P. and T.A. Michalske, *Accurate Method for Determining Adhesion of Cantilever Beams.* Journal of Applied Physics, 1999. **86**: p. 817-827.

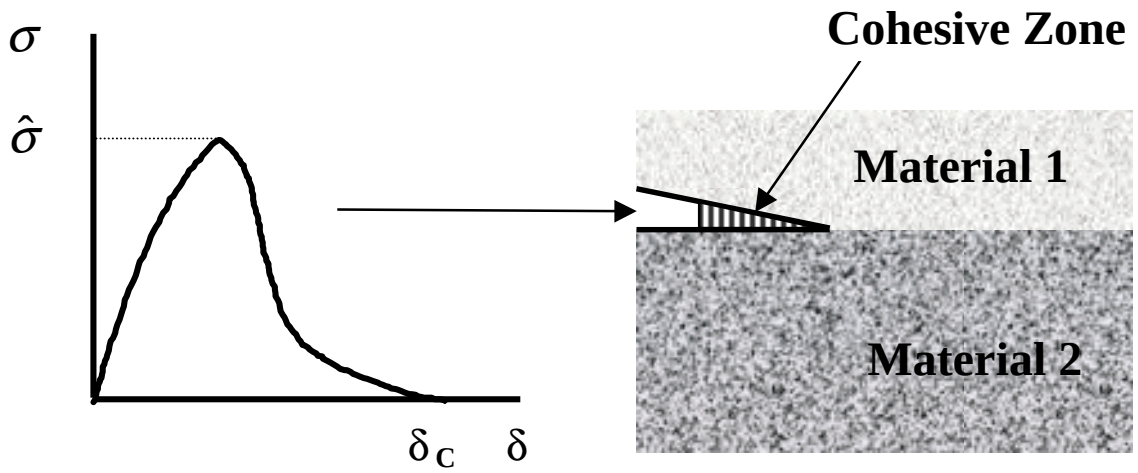

Figure 3.1. - Cohesive zone model for interfacial separation (adhesion), with behavior in the cohesive zone defined by a traction–separation (σ–δ) relation.

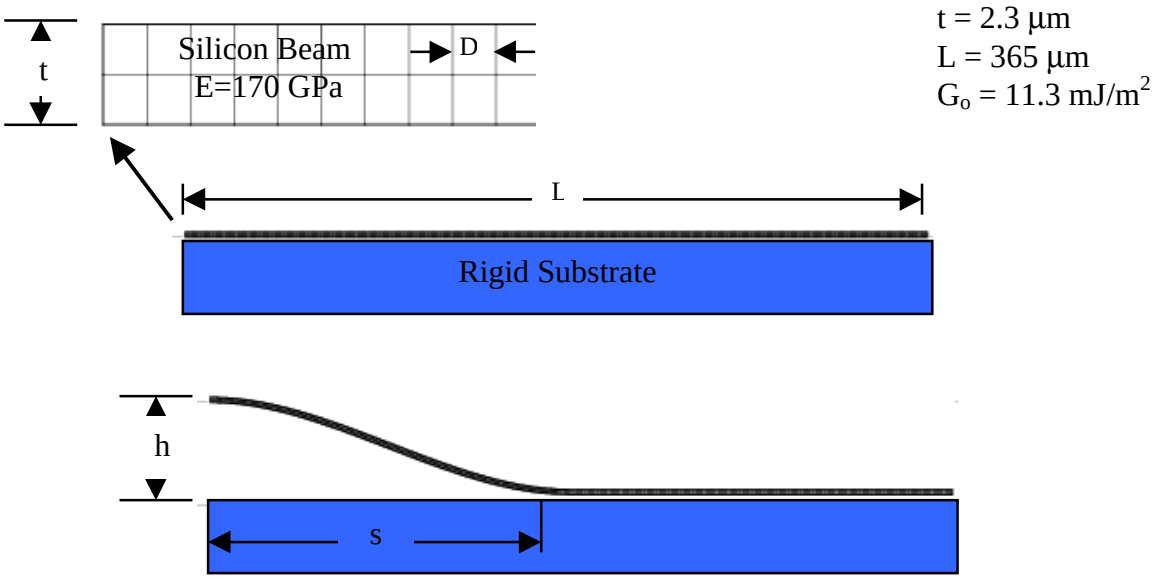

$$s = \left(\frac{3Eh^2t^3}{2G_o} \right)^{1/4}$$

Beam theory solution, de Boer & Michalske [11]

Figure 3.2. - Finite element model of a surface micromachined, cantilever beam adhesion test structure used by de Boer and Michalske (Ref. 3.11).

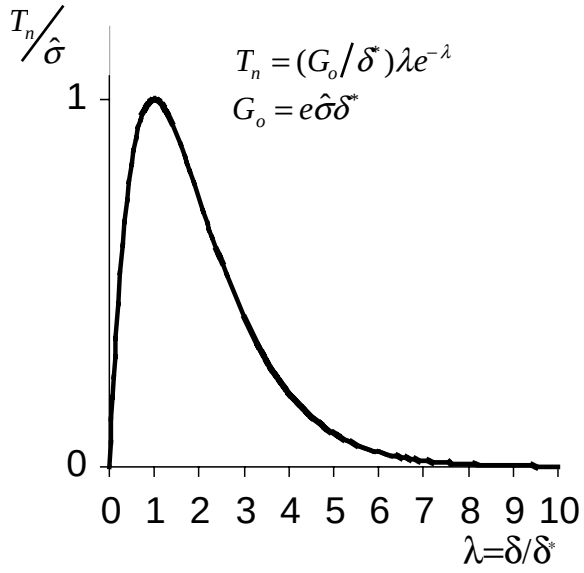

Figure 3.3. - Normal traction depends only on normal separation in the simplified version of the Xu-Needleman model (Ref. 3.10) used in adhesion test structure simulation.

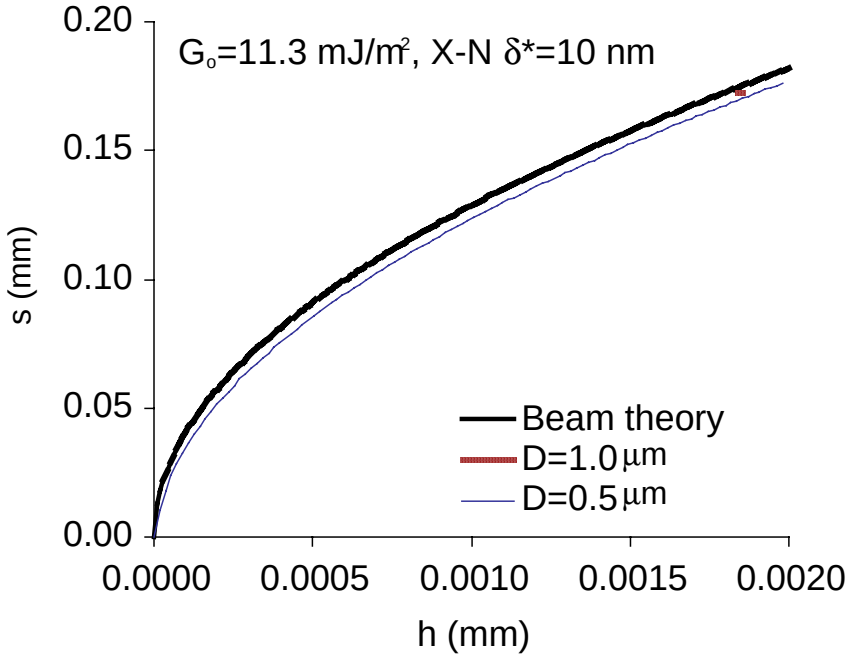

Figure 3.4. - Calculated nonadhered length vs. support post height of a surface micromachined, cantilever beam adhesion test structure.

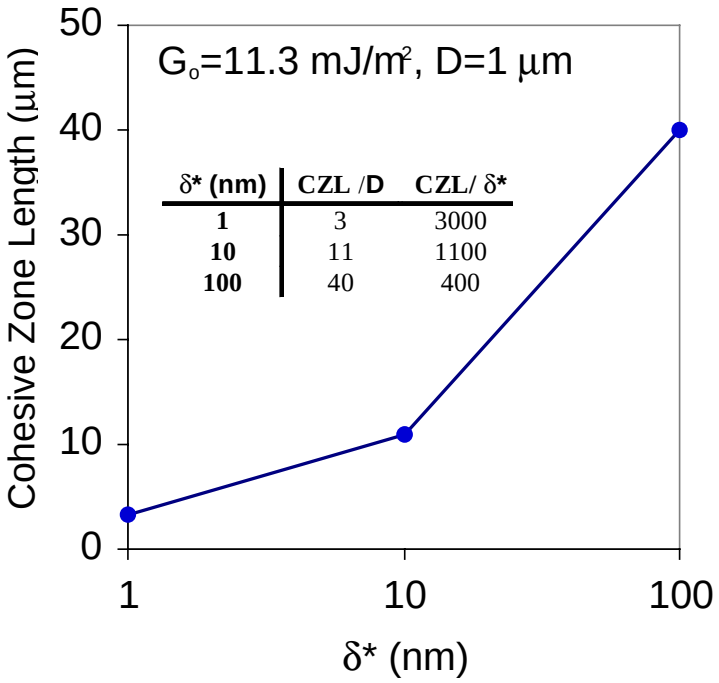

Figure 3.5. - Calculated cohesive zone length vs. the characteristic separation distance.

Figure 3.6. - Mesh used in the MEMS peel simulation (top silicon beam 100-μm long by 2.3-μm high by 1-μm deep).

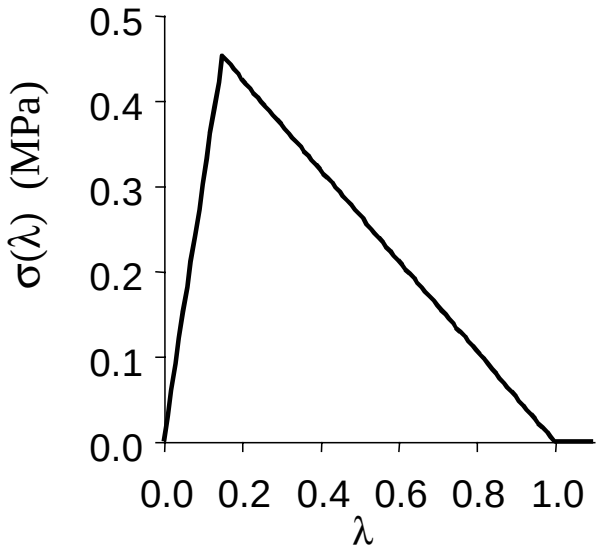

Figure 3.7. - The effective $\sigma(\lambda)$ relationship used in the MEMS peel simulation.

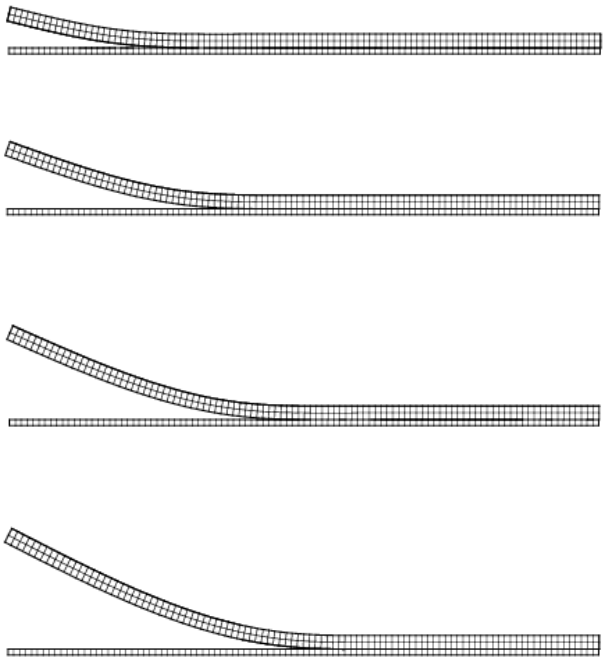

Figure 3.8. - Deformation of peeled strip (displacements magnified by 50x).

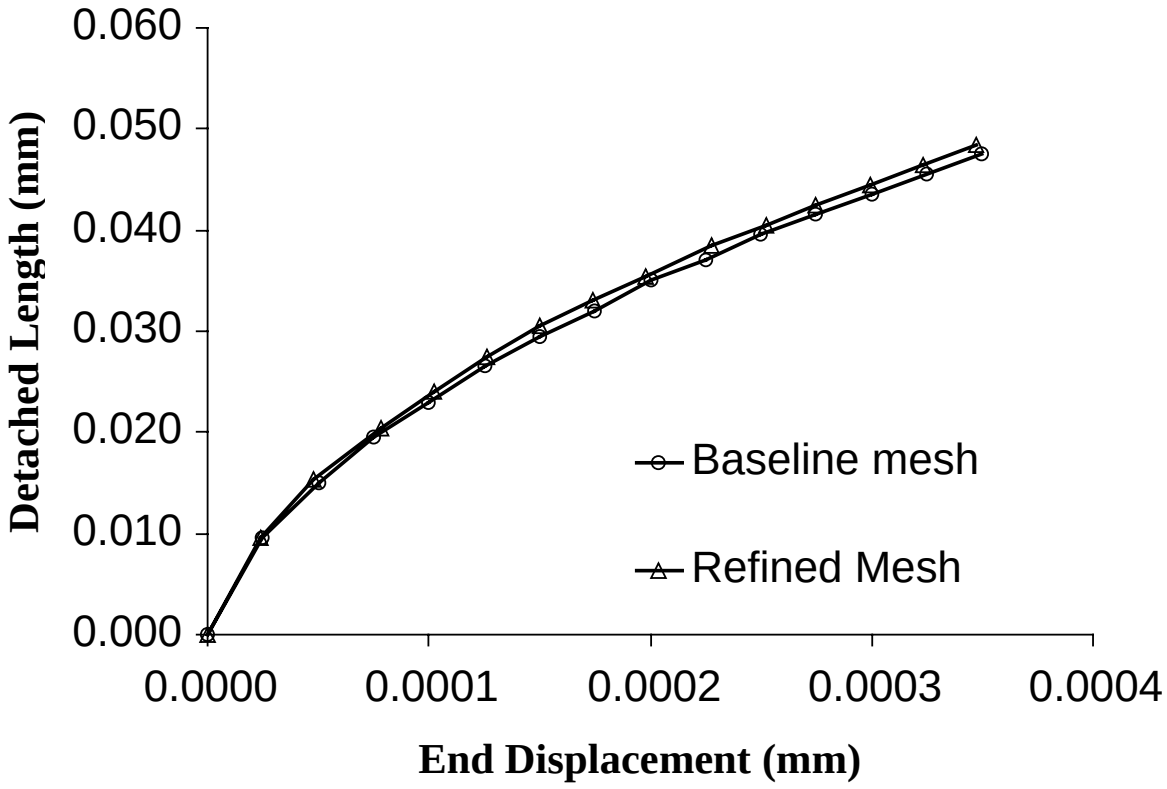

Figure 3.9. - Calculated crack length vs. end displacement for baseline and refined mesh.

4.0 EFFECT OF NANOTEXTURING ON INTERFACIAL ADHESION IN MEMS

4.1 INTRODUCTION

Polycrystalline (polysilicon) MEMS is a recently developed technology in which free standing thin film structures are actuated electrostatically to form micron-scale complex mechanisms such as resonating sensors, gears, linear racks, pop up mirrors, and mechanical logic (Ref. 4.1). Because of the large surface-to-volume ratio in this regime, surface forces can dominate over inertial forces, causing mechanisms to adhere rather than perform their intended function.

It is well known that increased surface roughness reduces adhesion of two contacting bodies. Models describing the effect of roughness on adhesion consider only the adhesion at (Ref. 4.2) or near (Ref. 4.3) areas of real contact. A reduction in adhesion due to enhanced roughness has also been observed in MEMS. For example, polysilicon roughening techniques have been used to reduce the tendency towards adhesion under wet conditions (Refs.4.4, 4.5). Free standing cantilevers were actuated under dry conditions and the transition from adhered to free cantilevers was detected to estimate adhesion values (Refs. 4.6, 4.7). It was observed that adhesion decreases with increasing surface roughness, and the authors suggested that $\Gamma \sim A/12\pi d_o^2$, where Γ is the adhesion (J/m^2), A is the Hamaker constant representing van der Waals forces, and d_o is the sum of the root mean square (rms) roughness of the two surfaces as measured by atomic force microscopy (AFM). Theoretical analysis considering the fractal nature of surfaces has also shown that adhesive forces decrease with increasing roughness (Refs. 4.8, 4.9).

In this work, we employ a joint experimental and modeling approach to address the effect of roughness on adhesion under dry conditions, allowing us to quantitatively address the following outstanding questions: (1) To what degree is MEMS adhesion controlled by areas of real contact versus by van der Waals forces across non-contacting portions of the surfaces? (2) What is the minimum achievable value of adhesion for contacting bodies with rough surfaces? (3) What is the optimum roughness in MEMS?

4.2 SAMPLE PREPARATION

Cantilevers were fabricated according to a three mask level process, schematically represented in Figure 4.1. Nanotexturing of the lower layer of polysilicon (poly 0 in Figure 4.1(a)) was accomplished by thermal oxidation in dry O_2 at 900 °C for increasing times. Table 4.1 indicates the times and the rms

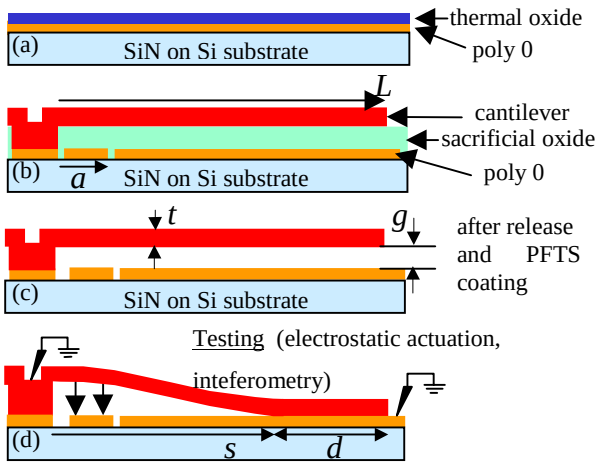

Figure 4.1. - (a) ground plane polysilicon (poly 0) oxidation (b) cantilever fabrication, (c) release and coating (d) testing

roughness as measured by AFM. Figure 4.2 shows SEM images of the surface textures achieved by this method after the release etch. Two features are noted. First, the main texturing effect is due to grains that protrude upwards from the surface. This occurs because the polysilicon grains are randomly oriented, and dry oxidation in the linear regime proceeds at different rates on different orientations of silicon (Ref. 4.10). Second, the grain boundaries are decorated at increasing oxidation times, giving rise to grooves. These do not contribute significantly to the desired texturing because they do not take up a large percentage of the surface area, and reach below the surface.

Table 4.1. - Polysilicon roughness versus oxidation time

Oxdn. Time (min)	Target tox (nm)	rms roughness (nm)
0	--	2.8
20	10	4.5
136	30	7.8
400	60	12.1

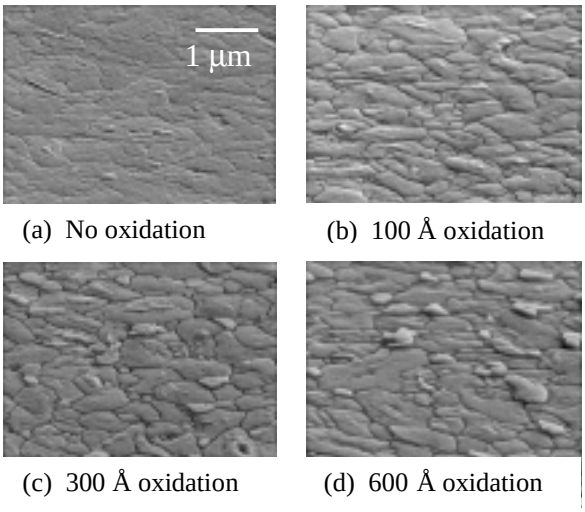

(a) No oxidation (b) 100 Å oxidation

(c) 300 Å oxidation (d) 600 Å oxidation

Figure 4.2. - Polysilicon ground plane surface textures versus oxidations times (SEM, 70° tilt).

Standard deposition, lithography and etch techniques were used to fabricate the cantilevers (Figure 4.1(b)). They are supported on the left in Figure 4.1 by a step-up support post, formed by filling a hole etched into the sacrificial oxide layer. A critical step is the release and coating of the cantilevers (Figure 4.1(c)). We used a solvent-based coating procedure that applies a self-assembled monolayer coating of perfluorodecyltrichlorosilane (FDTS, $C_8F_{17}C_2H_4SiCl_3$), similar to Ref. 4.7. Critical cantilever dimensions, as indicated in Figure 4.1, include gap height *g*, thickness *t*, width *w*, length *L*, and actuation pad length *a*. After actuation (Figure 4.1(d)), the length of the unattached region is used to denote the crack length *s*. Using profilometry, g=1.90 μm and thickness t=2.62 μm were determined from freestanding cantilevers. Mask dimensions were w=20 μm, a=81.5 μm and L ranged from 100 to 1635 μm.

4.3 ADHESION TEST RESULTS

Most cantilevers were free standing (not contacting the substrate) at lengths up to 1635 μm after the release and drying procedure as determined by interferometry. Some of these long cantilevers were contacting the substrate at their tips. In a few cases, cantilevers were attached over a relatively long length *d*, as indicated in Figure 4.1(d). This latter group was excluded from further analysis.

Knowledge of Young's Modulus E and torsional support post compliance β are critical to assessing Γ (Ref. 4.11). We used a procedure previously described in detail (Ref. 4.12) to determine E=163 GPa and β=1.25 μrad/(μN • μm). Also small curvatures

κ (caused by stress gradient through the thickness of the film) ranging from 0-1 m^{-1} were measured, and play a secondary role in determining adhesion values. These quantities are determined by electrostatically actuating the cantilevers, measuring the deflections and finding the best fit to finite difference models over a range of applied voltages.

Using a fracture mechanics analogy, a cantilever's adhesion to a substrate can be measured to high sensitivity and accuracy along its length (Refs. 4.11, 4.13). In the adhesion testing procedure, freestanding cantilevers are brought into contact with the substrate by modulating the voltage on the actuation pad. At low to moderate voltages (up to 60V for this geometry), the deflections are highly sensitive to interfacial forces acting between the cantilever and the substrate. The full deflection curve of the cantilevers is determined to better than 10 nm resolution.

For different voltages applied to the actuation pad, corresponding to different points of contact between the beam and the substrate, interferograms were taken and deflection curves were extracted. Knowing a and w from the mask layout and using the measured data for E, t, g, and β as input parameters, adhesion was determined by matching the model to each measured deflection curve. The only free parameter in the modeled curves is the adhesion Γ. A least squares fit between the model and measurement was used to determine its value. Typical minimum errors are less than 5 nm/pixel. Adhesion results for the different surface roughnesses are shown in Figure 4.3, where the squares (data) correspond to the measured values of adhesion. The adhesion data is plotted versus D_{av}, the average separation between the surfaces. For each value of D_{av}, Γ values were determined from two different cantilevers at applied voltages of 0, 10, 20, 30, 40, 50 and 60 V. Small systematic errors in the input parameters limit the absolute accuracy of the Γ values to ~10%, but will not affect the relative values of adhesion in Figure 4.3. Experimentally, the adhesion decreases only from 5.6 to 2.7 $\mu J/m^2$ over this roughness range.

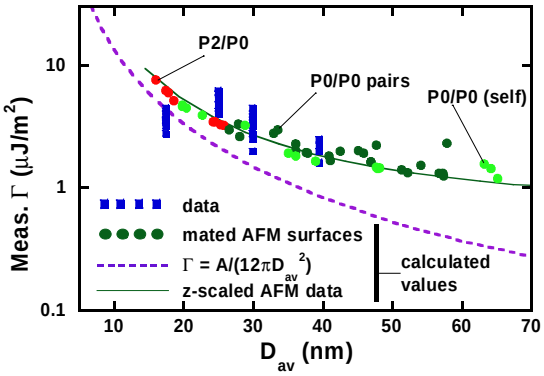

Figure 4.3. - Experimental and calculated results for adhesion versus average roughness.

4.4 ANALYSIS

Adhesion testing was conducted in air at ~30% relative humidity (RH). A contact angle of 110° of the FDTS coating with water was measured, indicating a hydrophobic coating. We have observed no effect of RH on testing results up to 80% RH for these coatings (Ref. 4.13). Therefore, capillary condensation, which dominates adhesion of hydrophilic surfaces (Ref. 4.14), does not play a role in these experiments. Furthermore, because the top and bottom surfaces are both grounded, electrostatic forces in the contact zone d are insignificant. However, externally applied loads, van der Waals forces between the surfaces and contact at asperities must be considered to analyze our results.

To model the interfacial forces, we measured the topography of the top and bottom surfaces by AFM (double-sided tape applied to the cantilevers allows them to be removed from the substrate and placed upside down for imaging). A question arises as to the area of the contacting region that should be modeled. By considering the free body diagram of the loaded cantilever, there must be a short region of compressive contact just beyond the crack tip. From simple beam mechanics, a point reaction force exists, but from elastic considerations, this region has length ~2*t*, and therefore the contact area should be considered is ~2*tw*=80 μm^2. In fact, 10x10 μm^2 AFM images with 256 or 512 pixels in each direction (e.g., 40 or 20 nm lateral resolution) were used in our analysis.

The AFM topograph data was read into a finite element program, and the top and bottom surfaces were placed in contact in various ways as will be described below. An elastic-plastic model was created to describe the silicon material with E=165 GPa and hardness H=12 GPa. However, it was soon found that for any reasonable pressure as applied by the external modulation, only the first contacting asperity in the contact zone deforms, and then by less than 0.5 nm. At each pixel, a parallel plate law for van der Waals forces was used to model the adhesive forces, similar to the equation posed in the Introduction, e.g., $\Gamma = A/(12\pi D_o^2)$. However, D_o now replaces d_o, where D_o represents the gap at each individual pixel, and the adhesion energy is summed up over the individual pixels and divided by the total area. For the few pixels where there is actual contact, a cutoff value of D_{oc} =0.3 nm (Ref. 4.15) was used. With $A=5 \bullet 10^{-20}$ J for a fluorocarbon surface, a surface energy of 15 mJ/m^2 is calculated in these regions. For comparison, values of 7 and 28 mJ/m^2 for advancing and receding surface energies respectively were recently determined by surface force apparatus measurements for a fluorocarbon surfactant (TAFC, $(C_8F_{17}C_2H_4)_2$-L-Glu-Ac-N^+-$(CH_3)_3$-Cl^-) applied to a mica surface.

The surfaces were placed in contact in various combinations. This included the original top and bottom measured layers with various random shifts in alignment, and pairs of the bottom layers including mating of the bottom layer to itself. The circles in Fig. 3 are the calculated adhesion results for the various combinations of the data. The solid line represents data from an individual placement combination, but with the roughness scaled to both lower and higher scales. The value of $D_{av} \approx 2d_o$ in Figure 4.3 is determined by the finite element analysis for a given placement of the top and bottom surfaces.

4.5 DISCUSSION

The abscissa D_{av} in Figure 4.3 is better used than d_o because it takes into account the actual alignment of the two surfaces, thereby reflecting the separation of the associated highest asperity pair. At small D_{av} values, $\Gamma = A/(12\pi D_{av}^2)$ is a good approximation for the calculated adhesion (circles in Figure 4.3). Of course, this equation will always be a lower bound for the adhesion values because of the non-linearity in this equation. However, as indicated by both the data and the model, the adhesion does not fall off with $1/D_{av}^2$ at large D_{av} values. It is important to realize that

for these deposited layers, there is no long-range waviness to the surfaces. Therefore, surfaces can be near each other over large distances without contacting.

To qualitatively understand the results, we consider two conceptual extremes in the adhesion between rough surfaces. In one, the surfaces are relatively smooth and contact is at only one asperity point. Van der Waals forces across non-contacting portions of the surfaces, whose area is far greater than the contacting area at the one asperity, will dominate the adhesion in this case. For example, at D_{av} =10 nm, Γ=13 μJ/m^2 is expected as seen in Figure 4.3. At the other extreme, the surfaces are rough, and D_{av} is large. Only the single point of contact contributes to the adhesion. In this case, we would expect $\Gamma \sim (AR/(6D_{oc})/L_c^2)$, where R is the radius of the contacting asperities and L_c^2 is the area of adhesion that is being probed (the term $AR/(6D_{oc})$ is the van der Waals adhesion energy between two contacting spheres). With R=50 nm as a typical value for the polysilicon asperities in these experiments and L_c^2=100 μm^2 as discussed above, we expect a lower bound for adhesion to be 0.014 μJ/m^2. This latter extreme is a simplified expression of the Maugis model of rough surfaces (Ref. 4.3), which takes van der Waals forces into account, but only at contacting asperities. That model is more appropriate here than the Fuller-Tabor model (Ref. 4.2) because of the large E, small R and low energy of these surfaces. Note that the values of adhesion in Figure 4.3 are much closer to the former than the latter extreme, implying that van der Waals forces over non-contacting areas dominate the adhesion. Negligible adhesion hysteresis measured in other experiments corroborates this notion (Ref. 4.13).

To quantitatively understand the results, consider Figure 4.4, where a histogram of the relative contributions from the range of D_o values is plotted for different surface roughnesses. At small D_{av}, most of the contribution to adhesion comes from non-contacting surfaces, whereas at large D_{av}, the contribution from surfaces nearly in contact begins to become the largest contributor.

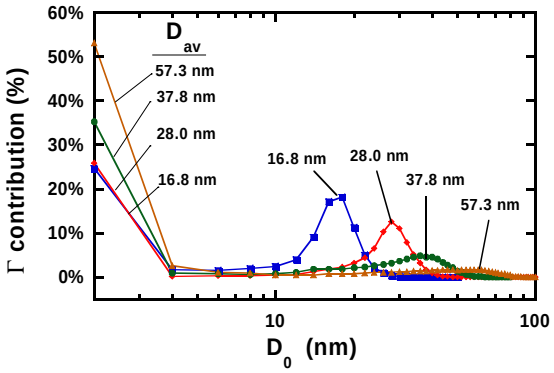

Figure 4.4. - Calculated relative contributions to the adhesion versus gap at each location.

We can now address the questions posed in the Introduction. (1) Typically, MEMS surfaces exhibit D_{av} ~10-30 nm. Therefore, most adhesion in MEMS is due to van der Waals forces between non-contacting areas. Even for large D_{av} in Figure 4.3, this remains true - The reason for the small reduction in Γ is that nearby non-contacting asperities begin to contribute significantly. As D_{av} grows large (above 60 nm), the Maugis model will begin to adequately describe the adhesion, because the contribution to Γ of D_o near 0 grows. (2) Adhesion as low as 0.01 μJ/m^2 should be possible by making surfaces rough. However, because of the weak dependence of Γ on D_{av}, extremely large

roughness would be required. Given that MEMS structures are often used for optical reflection in mirror applications, this would be an unpopular choice. (3) There is a deviation in the calculated curve from $\Gamma = A/(12\pi D_{av}^2)$ beginning at D_{av} ~25 nm. We suggest this is a near-optimal separation value. For lower values of roughness adhesion begins to increase significantly because of the close proximity of the surfaces, while for large values of roughness optical reflectivity is significantly compromised.

Using the Greenwood-Williamson model (Ref. 4.16), which applies reasonably well for these surfaces, the ratio of real to apparent contact area is found to be approximately 10^{-8} for the smoothest surfaces. The real contact area is greatly overestimated in the finite element formulation because of the pixel size limitation. Depending on the lateral resolution used in the AFM measurements, the smallest possible ratio is $(1/256)^2=1.5 \bullet 10^{-5}$ or $(1/512)^2=3.8 \bullet 10^{-6}$. Because the contribution to the total adhesion of the contacting point is still small, this causes only a small error in the adhesion calculation. However, this is further evidence that van der Waals forces in the vast area between contacts dominates the adhesion of these surfaces, especially when the average separation is small.

4.6 SUMMARY AND CONCLUSIONS

Understanding the effects of surface roughness on parameters such as adhesion, friction and wear is a central question in the tribology of MEMS. By combining deflection data from interferometry with computer-based models, the use of as-fabricated MEMS test structures provides a powerful means to the assess the interfacial adhesion between rough surfaces. In this work, we fabricated polysilicon cantilevers over textured surfaces of varying nm scale roughness, and measured the interfacial adhesion of the cantilevers to the surfaces. Contrary to expectations, the effect of roughness, when increased over a large range from 3 to 12 nm rms, reduced the adhesion only by a factor of 2, instead of by a factor of 16 as expected from previous literature models. We studied adhesion by inputting 3-D data from AFM topographs of the surfaces into a finite element code, and mating the surfaces in the computer. It was found that at small roughness values, adhesion is mainly due to van der Waals forces across non-contacting areas and is proportional to 1/(average surface separation)^2. At large roughnesses, asperities that nearly bridge the gap are the dominating contributor to the adhesion.

4.7 ACKNOWLEDGMENTS

We thank the Microelectronics Development Laboratory at Sandia National Laboratories for processing the samples. We thank Aaron Hall for help in obtaining AFM data.

4.8 REFERENCES

4.1 J. J. Sniegowski and M. P. de Boer, Annu. Rev. Mater. Sci. **30** 297 (2000).
4.2 K. N. G. Fuller and D. Tabor, Proc. Roy. Soc. Lond. A. **345** 327 (1975).
4.3 D. Maugis, J. Adh. Sc. Tech. **10** (2) 161 (1996).
4.4 R. L. Alley, P. Mai, K. Komvopoulos and R. T. Howe, Proc. 7th Int. Conf. Solid-State Sensors and Actuators, Transducers '93, Yokohama, Japan, 1993, pp. 288-291.

4.5 Y. Yee, K. Chun and J. D. Lee, The 8th Int. Conf. on Solid-State Sensors and Actuators, Transducers '95, Stockholm, Sweden, 1995, pp. 206-209.
4.6 M. R. Houston, R. T. Howe and R. Maboudian, J. Appl. Phys. **81** (8) 3474 (1997).
4.7 U. Srinivasan, M. R. Houston, R. T. Howe and R. Maboudian, J. Micromech. Sys. **7** (2) 252 (1998).
4.8 K. Komvopoulos and W. Yan, J. Trib. **119** 391 (1997).
4.9 K. Komvopoulos and W. Wan, J. Appl. Phys. **84** (7) 3617 (1998).
4.10 *VLSI Technology*; *Vol.* , edited by S. M. Sze (McGraw-Hill, New York, 1983).
4.11 J. A. Knapp and M. P. de Boer, J. MEMS, **submitted** (2001).
4.12 B. D. Jensen, M. P. de Boer, N. D. Masters, F. Bitsie and D. A. LaVan, J. MEMS **10** (3) pp. 336-346 (2001).
4.13 M. P. de Boer, J. A. Knapp, T. A. Michalske, U. Srinivasan and R. Maboudian, Acta Mater. **48** (18-19) 4531 (2000).
4.14 M. P. de Boer, P. J. Clews, B. K. Smith and T. A. Michalske, Mater. Res. Soc. Proc., San Francisco, CA, 1998, pp. 131-136.
4.15 J. Israelachvili, *Intermolecular and Surface Forces* (Academic Press, New York, 1992).
4.16 J. A. Greenwood and J. B. P. Williamson, Proc. Roy. Soc. Lond. A. **295** 300 (1966).

5.0 NONCONTINUUM THERMAL TRANSPORT

5.1 INTRODUCTION

The continual process of adding functionality while reducing size, characteristic of microsystem development, generally implies increased heat generation coupled with a smaller area over which to dissipate it. Higher operating temperatures, however, tend to degrade performance and shorten life. Compounding this problem, several experiments have shown that the effective thermal conductivity of solid materials decreases as their characteristic lengths become very small (typically sub-micron) or characteristic times become very short (typically sub-picosecond). Consequently, as devices shrink, thermal predictions from macroscale tools will rapidly depart from observed values. Already, predicted and measured thermal conductivities have been shown to differ by more than an order of magnitude in the superlattices critical to vertical-cavity surface-emitting lasers (VCSELs) (Ref. 5.1). Furthermore, thermal conductivity becomes anisotropic when the characteristic dimension depends on direction, which can significantly change the heat flow pattern, in addition to its magnitude.

As microsystems become more complex, accurate modeling at the design stage becomes more important to their success. In addition, because these devices rely on relatively new technology, their degradation due to aging and their performance in extreme environments are still largely unknown. It is therefore critical to understand thermal processes at a level sufficient to not only predict where the current models fail, but to extend the models to function in the unexplored regime. This consideration is also important for evaluating commercial off-the-shelf (COTS) components for use in the stockpile and in other applications that imply requirements not foreseen (or tested) by the manufacturer.

5.2 OBJECTIVES

This effort is intended to produce models that can accurately represent thermal transport in microdevices. For moderately miniaturized devices, it should be possible to employ existing macroscale models with modified transport coefficients. In the long term, as devices become smaller, an entirely microscale viewpoint will be required. Consequently, this effort was split into two parts: (1) extension of current tools for application in limited regions of the microregime and (2) creation of new tools that have predictive capability throughout this regime.

For the former task, a goal was set to modify existing codes to accommodate anisotropic transport coefficients and assess their applicability to devices of interest. This involves analyzing the thermal response of an existing MEMS component under a normal operation condition using the ‘best-estimate’ anisotropic heat conduction coefficient.

For the latter task, a long-term goal was set to create a new tool that could function in concert with existing codes. The resulting hybrid tools would then not only be accurate in both macro and micro regimes, but also efficient for devices that bridge both regimes. A nearer-term objective was to evaluate existing models with respect to the long-term goal to ensure the optimal model was adopted, adapted, or created for the new tool.

5.3 SUMMARY OF PROGRESS

5.3.1 Macroscale Tool Modification

There is a significant interest in the DOE Defense Program (DP) community to evaluate and demonstrate microsystem technology to enhance surety and performance of various components in the nuclear weapon (NW) systems. This motivation has lead to a microsystem product-realization effort at Sandia to design a relevant microsystem, profoundly understand its behavior over time and within a variety of environments, and fully characterize all fabrication, micro-assembly, and packaging processes.

The first phase of this realization process is to build and test a product emulator, which is a micro-switch. This switch system has an optical shutter, a vertical-cavity surface-emitting laser (VCSEL), a photo-detector (PD), and a microprocessor. The optical shutter is a 500-μm-diameter disc with an off-center hole (Figure 5.1). When the hole is positioned and aligned with the optical path of the VCSEL and the PD, light is detected and an electric current is generated. Thus the switch will be on. When the hole is rotated leading to a misalignment, the switch will be off. This is the first generation of the MEMS design. However the challenge is to package the system as an integrated unit, demonstrate its functionality and reliability, and qualify its performance under various conditions. Since SMM is a relatively new technology, modeling and simulation as well as testing will be applied to analyze the response of this micro-switch under various conditions.

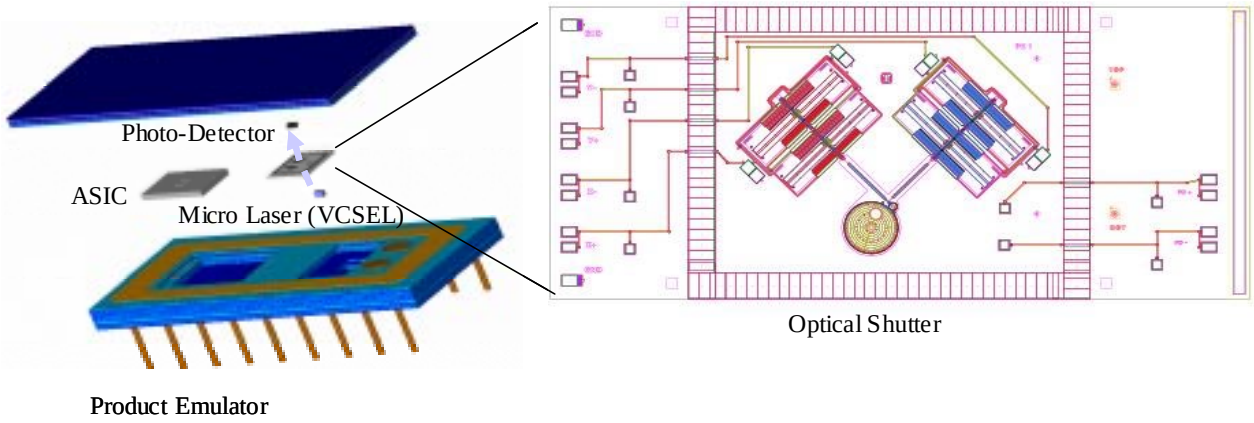

Figure 5.1. - Schematic picture of the product emulator.

A thermal analysis is needed in order to investigate the thermal response of the optical shutter as a result of the spot heating from the VCSEL. During normal operation, the VCSEL will be turned on for a period of time before the optical shutter is rotated to the ‘on’ position. This leads to a concern about thermal loading on the optical shutter, i.e. increases in temperature and induced thermal stresses.

Investigation of the Thermal Response of an Optical Shutter

To model the spot heating from the micro-laser, we need to imprint a circle on the bottom surface of the optical shutter in order to impose a heat flux boundary condition. This setup implies that the 'Design-to-Analysis' software package for microsystem analysis needs to be flexible and adaptive.

The first thermal analysis is based on the COYOTE prediction utilizing the thermal conductivity of bulk silicon. It shows that the temperature distribution is relatively uniform because bulk silicon is a very good heat conductor (Figure 5.2).

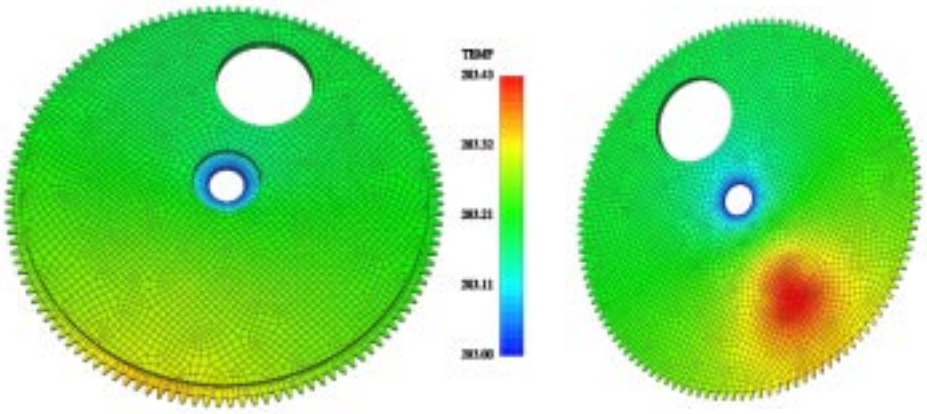

Top Bottom

Figure 5.2. - Predicted temperature profile of the optical shutter using the bulk silicon thermal conductivity.

It is known that the thermal properties of polycrystalline silicon can be process-dependent. In the SUMMiT™ process, there are multiple processing steps, which involves doping and annealing. That implies that the thermal properties of the polysilicon in the optical shutter can be quite different from the bulk silicon. If we use the measured thermal conductivity of the undoped polycrystalline silicon without any annealing from Ref. 5.2, i.e. 10 W/m·K instead of 157 W/m·K, a non-uniform temperature distribution is predicted (Figure 5.3). The moderate difference in temperature distribution of the optical shutter implies that the optical shutter may not stay flat as expected. Thus a thermal stress analysis may be valuable.

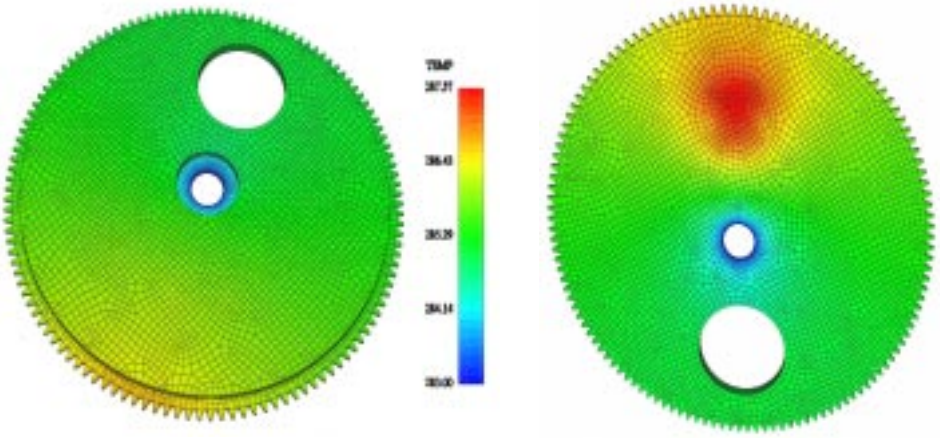

Top Bottom

Figure 5.3. - Predicted temperature profile of the optical shutter using the undoped polysilicon thermal conductivity.

5.3.2 Microscale Tool Development

Thermal transport at the microscale is best viewed in terms of the behavior of heat carriers, which are predominantly electrons in conductors and phonons (lattice vibrations) in semiconductors and insulators. As the characteristic length shrinks, scattering between heat carriers becomes less important and their travel becomes increasingly ballistic. Heat transfer thus transitions from a diffusive to a convective phenomenon.

If the wave character (the phase, in particular) of the carriers can be neglected, the Boltzmann transport equation (BTE) provides a good model for microscale transport because it explicitly represents scattering and ballistic flight. Unfortunately, this seven-dimensional integro-differential equation has proven difficult to solve, even numerically, for realistic problems. As a result, previous researchers in this area have applied a wide variety of simplifications and numerical techniques. These efforts were evaluated with respect to the current goals and the primary candidates are discussed below. The method chosen for the current work is then described and preliminary results are provided.

Previous Work

Majumdar (Ref. 5.3) derived perhaps the most general solution of the BTE for phonons by transforming the distribution function into intensity to produce the "equation of phonon radiative transfer" (EPRT), so named due to its similarity to the ERT commonly used in radiation modeling. To make the solution tractable, however, he assumes an overall radiative equilibrium at each frequency. The limitations of this assumption have not been investigated.

Starting from the EPRT, Chen (Ref. 5.4) derived another formulation by splitting the intensity into components contributed by ballistic transport from the boundaries and diffusive transport from the surrounding material. It is not clear, however, how to

include partial accommodation at the interfaces and the method becomes quite complex if temperature-dependent relaxation times are included.

In an effort to capture the effects of propagation speeds dropping to zero for high frequency phonons, which become more important as the temperature increases, Sverdrup, Ju and Goodson (Ref. 5.5) divide the carriers into propagating and reservoir modes. They then derive an equation very similar to the EPRT by writing the BTE in terms of excess phonon energy density over a reference state. Their radiative equilibrium-type assumption is more easily justified than Majumdar's but they then assume a constant heat capacity, which is only true for small temperature variation or very large temperatures.

Finally, Guyer (Ref. 5.6) developed a lattice Boltzmann model for heat conduction in cryogenic systems. Notably, he avoided the relaxation time-based collision operator (BGK) used in all the other methods in his first attempt. This resulted in spurious waves in transient solutions because he neglected non-momentum-conserving (Umklapp) processes, which become important at higher temperatures. In addition, Guyer did not include boundaries in his calculations, showed no comparisons to experimental data, and only 1D results were presented (though the formulation was 2D).

Chosen Approach

Based on the analysis of previous work in modeling microscale heat transport, lattice Boltzmann (LB) was chosen as the most promising technique due to its advantages in terms of flexibility and computational efficiency.

Flexibility is gained from the relatively small number of assumptions required to construct the method. Furthermore, it is straightforward to make the relaxation time at a node dependent on the local "temperature" and on frequency. This may be an important feature because functional dependencies as high as a fourth and second power on temperature and frequency, respectively, have been suggested in the literature (Ref. 5.7). Finally, the BGK assumptions made by all the non-LB methods could possibly be replaced with a term involving products of local distribution functions, which is closer to the actual Boltzmann equation collision term.

Efficiency is gained over the particle methods often proposed for microscale transport calculations via an ability to calculate macroscale variables directly from grid quantities instead of by collecting statistics on them. This ability greatly reduces sampling time and enables a coupling to continuum codes without injecting statistical noise. Lattice Boltzmann, however, retains the particle methods' ready parallelizability and extensibility to multiple dimensions. In addition, complex domain shapes are trivial due to its Cartesian grid and subgrid-scale geometric variations may be modeled if the "partially-filled cell" techniques (Ref. 5.8) used in LB fluid simulations can be adapted for heat carriers.

The remaining time on this task was spent developing a proof-of-concept code to demonstrate LB's feasibility in this context and to flush out issues that may affect its viability as a long-term solution. The first-cut code uses a D2Q4 model, meaning it is 2D and uses four velocities. These velocities have identical speeds and point along the Cartesian directions. The temperature is taken as proportional to the fourth root of the

total phonon energy. This definition relates the total energy to that of a Bose-Einstein distribution at the reported temperature. The fourth-root relationship is strictly valid only at very low temperatures, becoming a more complex relationship at higher temperatures as the finite range of allowable phonon frequencies becomes increasingly important.

Sample results from the proof-of-concept code are shown in Figure 5.4. These results show that even the simplest baseline model is able to reproduce diffusive-dominated heat transport, characteristic of most macroscale devices and modeled by Fourier's law, as well as ballistic-dominated heat transport, characteristic of deeply microscale devices.

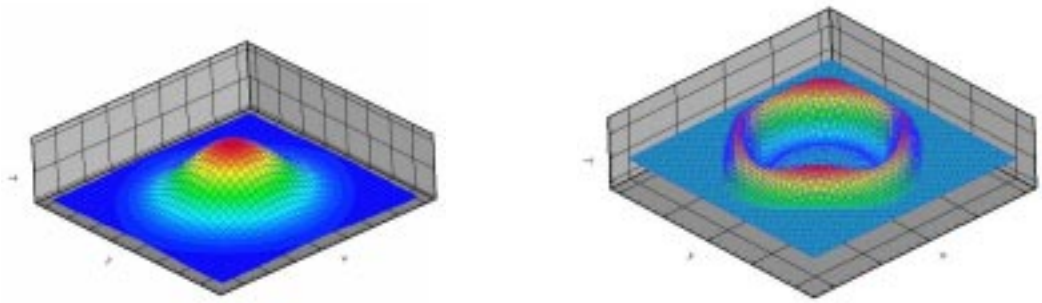

(a) (b)

Figure 5.4. - Demonstration of (a) diffusive-dominated and (b) ballistic-dominated heat transport following a short-duration energy input at the domain center.

5.4 PLANS FOR FUTURE DEVELOPMENTS

5.4.1 Macroscale Tool Modification

We will continue to evaluate the measured thermal properties of polysilicon due to the variation of the surface micromachining process. These thermal properties will be used in the continuum model to predict thermal response of the microsystems.

5.4.2 Microscale Tool Development

We will continue to develop the microscale tool, progressing to a model for thin films that can predict transport coefficients as a function of film thickness, material, and processing. From this point, more complex devices will be treated, starting with essentially 2D structures, such as the hotspots surrounding microfabricated transistors discussed by Sverdrup *et al.* (Ref. 5.9), and moving to fully 3D geometries.

5.5 REFERENCES

5.1 G. Chen and M. Neagu. Thermal conductivity and heat transfer in superlattices. *Applied Physics Letters*, 71(19):2761-2763, Nov 1997.

5.2 Asheghi, M., Kurabayashi, K., Goodson, K.E., Kasnavi, R., and Plummer, J., "Thermal Conduction in Doped Single-Crystal Silicon Films," Proceedings of the 33rd National Heat Transfer Conference, Albuquerque, NM, August 15-17, 1999.

5.3 A. Majumdar. Microscale heat conduction in dielectric thin films. *Journal of Heat Transfer*, 115:7-16, Feb 1993.

5.4 G. Chen. Ballistic-diffusive heat-conduction equations. *Physical Review Letters*, 86:2297-2300, 2001.
5.5 P.G. Sverdrup, Y.S. Ju, and K.E. Goodson. Sub-continuum simulations of heat conduction in silicon-on-insulator transistors. *Journal of Heat Transfer*, 123(1):130-137, Feb 2001.
5.6 R.A. Guyer. Phonon gas: a lattice Boltzmann description. *Physical Review E*, 50(6):4596-4608, Dec 1994.
5.7 P.G. Klemens. Thermal conductivity and lattice vibrational modes. In F. Seitz and D. Turnbull, editors, *Solid State Physics*, Volume 7, Pages 1-98. Academic Press, NY, 1958.
5.8 D.R. Noble and J.R. Torczynski. A lattice-Boltzmann method for partially saturated computational cells. *International Journal of Modern Physics C*, 9(8):1189-1201, Dec 1998.
5.9 P.G. Sverdrup, S. Sinha, M. Asheghi, S. Uma, and K.E. Goodson. Measurement of ballistic phonon conduction near hotspots in silicon. Applied Physics Letters, 78(21):3331-3333, May 2001.

6.0 NETWORK ALGORITHMS FOR MINIMUM ENERGY FRACTURE SURFACES

6.1 INTRODUCTION

The Griffith criterion gives the minimum energy E_f that must be expended to break a homogeneous solid body into two pieces. That energy is simply the free energy required to form two new surfaces

$$E_f = \Delta EA \tag{6.1}$$

where ΔE is the surface formation energy per unit area and A is the surface area of the fracture. In a homogeneous body, ΔE is the energy of forming two new surfaces from the bulk, 2σ, where σ is the surface free energy per unit area. Since the fracture area is assumed minimum, the crack must be planar, and A is the cross-sectional area of the sample.

The Griffith criterion is strictly thermodynamic. Kinetic processes such as plasticity, crack branching, crack bridging and healing all add to the fracture energy. However, the Griffith criterion provides a useful baseline energy below which fracture cannot occur.

The two assumptions of the Griffith theory are a homogeneous medium and a planar fracture surface. In typical metallic and ceramic materials, both assumptions fail. Most metals and ceramics solids are comprised of individual crystallites, called grains. Grain boundaries are the internal interfaces between these crystallites. These boundaries are generally weaker (lower fracture energy) than the bulk material, which negates the homogeneity assumption. In addition, the fracture surface deviates to seek out these low energy paths, which invalidates the planarity assumption.

For fracture along grain boundaries (intergranular fracture), the production of new surface (at a cost 2σ) occurs simultaneously with the elimination of a grain boundary (of energy per unit area γ). Thus ΔE is the sum of surface formation and interface destruction terms,

$$\Delta E = 2\sigma - \gamma \tag{6.2}$$

The challenge of determining the Griffith criterion for intergranular fracture then becomes finding the fracture area A. In this paper, we utilize network algorithms to determine A for intergranular fracture in two-dimensional and three-dimensional (3D) equiaxed polycrystals.

6.2 FRACTURE MODEL

Polycrystalline grain structures form natural networks. For example, in two dimensions (2D) the grain boundaries themselves form a graph where grain boundaries are edges, and grain junctions are nodes, as shown in Figure 6.1(a). Alternately, a graph may be drawn by connecting the centroids of neighboring grains, as shown in Figure 6.1(b). This grain connectivity graph is the dual of the grain boundary graph; it is also useful to note that while the grain boundary graph is valid only in 2D, the grain connectivity graph is general.

In both representations of the grain structure, each edge has weight $W_e = \Delta E_e l_e$, where l_e is the length of the boundary and ΔE_e is the surface formation energy per unit length of that boundary.

To find the Griffith energy for intergranular fracture, we must identify a surface that divides a polycrystal into two parts while conforming to the grain boundaries and minimizing surface formation energy. Such surfaces may be found by various network algorithms. In 2D, Djikstra's algorithm finds the single-source shortest path across the grain boundary graph (Ref 6.1). Since the edge weights are the surface formation energies, the shortest path across the graph is the intergranular fracture surface of minimum formation energy.

To solve the 3D problem, we use the grain connectivity graph. This graph is a capacitated network, defined as a graph consisting of nodes, edges which connect nodes, and capacities associated with each edge. The top and bottom surfaces of the sample are defined as source and sink nodes. The maximum flow (max-flow) a network can sustain is the largest numerical flow that can move from the source to the sink, node to node via the connecting edges, with no edge carrying more flow than its capacity. The minimum cut (min-cut) is the separation of the network into two networks, with the source in one new network and the sink in the other, such that the sum of the capacities of the broken edges is minimal. Ford and Fulkerson (Ref. 6.2) proved that the max-flow in a network occurs across the min-cut and developed a polynomial-time algorithm to determine the max-flow. Edmonds and Karp (Ref. 6.3) modified the algorithm to guarantee convergence in the case of non-integer capacities.

The max-flow/min-cut algorithm proceeds by associating a flow value with each edge in the network, initially set to zero. An attempt is made to push an infinite amount of flow out of the source, limited by the flow available in the edges leaving the node. This process is repeated for each node reached by the new flow until some incremental flow reaches the sink. When this happens the flow values of all edges in the path that this new flow took are updated to reflect the increase. This procedure is repeated, each time augmenting the flow from the source to the sink, until a path to push even the smallest flow increase to the sink cannot be found. The resulting flow reaching the sink is the max-flow, and also the value of the min-cut.

For a grain structure graph, the minimum surface formation energy fracture is the surface that divides the graph into two pieces while cutting edges with the minimum total edge capacity, i.e. the min-cut. Therefore, the max-flow/min-cut algorithm can provide both the position and surface formation energy for the minimum energy fracture.

All grain structures in this study were equiaxed, single-phase polycrystalline microstructures produced using a 3D Monte Carlo Potts Model grain growth simulation (Refs. 6.4-6.6). Although the fracture model can operate on digitized experimental microstructures, simulated microstructures were used to allow a 3D representation and to ensure statistical equivalence between specimens. Because we are interested only in surface formation energy, we ignore mechanical processes in crack propagation, including plasticity, crack branching, crack bridging and healing.

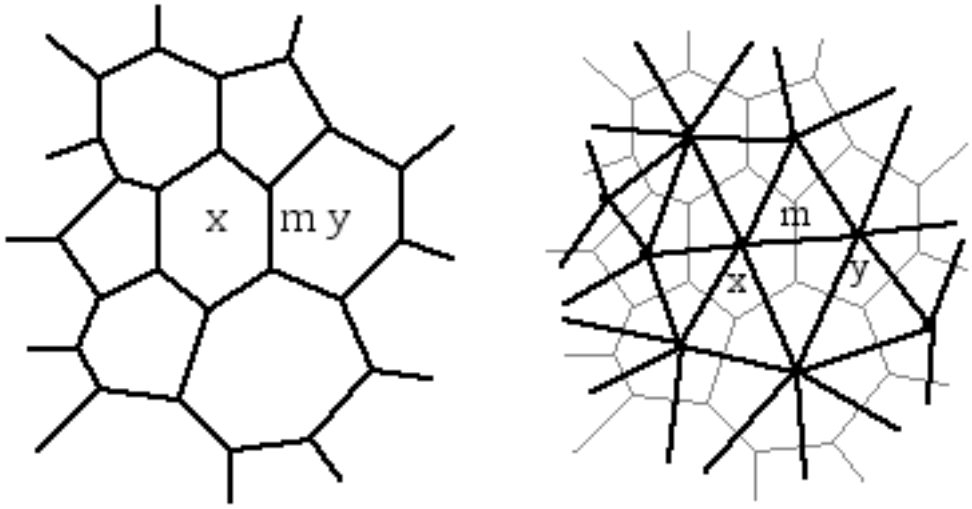

(a) (b)

Figure 6.1. - Grain structures represented as networks. (a)Grain boundary network. Edges (black lines) are grain boundaries, nodes occur at boundary junctions. (b)Grain connectivity network. Nodes of the graph are the grain centroids; edges (black lines) connect centroids of neighboring grains. (Gray lines indicate the background grain structure.) In both cases, the boundary between grains *x* and *y* has surface formation energy of *m* units.

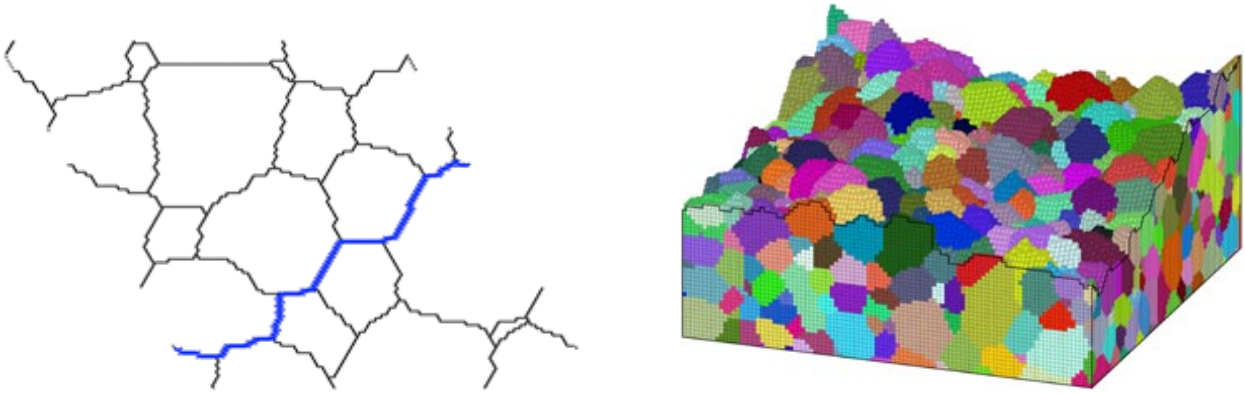

(a) (b)

Figure 6.2. - Intergranular fracture surfaces of minimum surface formation energy for equiaxed polycrystals with uniform boundary strength. (a) In 2D the heavy line indicates the fracture surface. (b) In 3D the fracture surface is the top surface drawn.

6.3 EQUIAXED POLYCRYSTALS

The simplest case of intergranular fracture occurs in equiaxed polycrystals with very weak (i.e. high-energy) grain boundaries. In that case, there are no directional effects due to elongated or non-compact grain shapes, and there is no competition between cleavage and intergranular fracture modes.

Figure 6.2 shows typical intergranular fracture surfaces of minimum surface formation energy in 2D and 3D equiaxed grain structures with uniform, weak boundaries. The cracks form relatively smooth surfaces, and interlocking grain configurations are absent.

As shown in Figure 6.3, a 2D path 1.1 times as long as its end-to-end width extrapolates to a 3D surface of area 1.2 times the cross-sectional area. Actual 3D fracture surfaces are of considerably larger area. This indicates that 2D and 3D fracture surfaces are fundamentally different. This is not surprising considering the difference in boundary topology in two and three dimensions. In particular, the requirements of connectivity prevent each slice of the 3D surface from being a minimum length 2D path. Since the 3D minimum energy fracture is not a composite of 2D minimum fractures, its area is necessarily larger than that extrapolated from the 2D results.

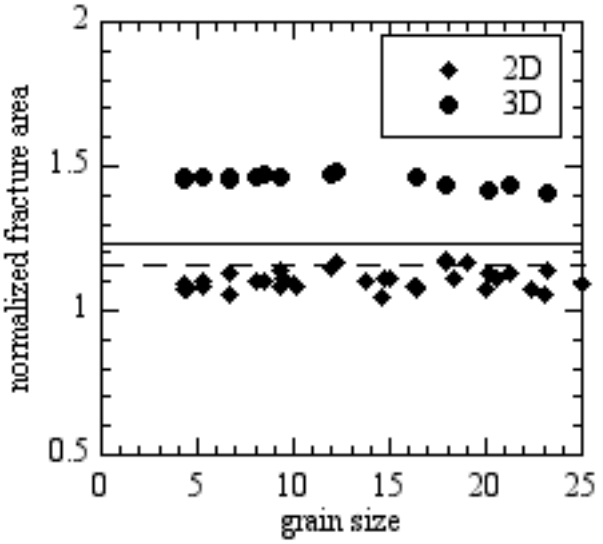

Figure 6.3. - Minimum surface formation energy intergranular fracture surface size as a function of equiaxed grain size in 2D (diamonds) and 3D (circles). Fracture size is shown normalized by the sample width (2D) or cross-sectional area (3D). Fracture size does not change with grain size. In 2D, fracture length is approximately the same as for a perfect hexagonal grain array (dashed line). In 3D, fracture area is much larger than extrapolated from the 2D result (solid line).

6.4 MICROCRACKED POLYCRYSTALS

Anisotropic thermal expansion of crystalline grains can cause inhomogeneous stresses at grain boundaries. During cooling after processing, these stresses can cause weakening or even cracking of individual grain boundaries. This phenomenon is termed microcracking, and it can drastically alter the fracture morphology.

We consider a system in which special boundaries have a surface formation energy ΔE_s which is much lower than the surface formation energy for normal boundaries ΔE_n;

here $\Delta E_s = 0.01 \Delta E_n$. We assign a fraction f of the boundaries in the system at random to be special boundaries, so the average surface formation energy in the system is $\langle \Delta E \rangle = f \Delta E_s + (1 - f) \Delta E_n$.

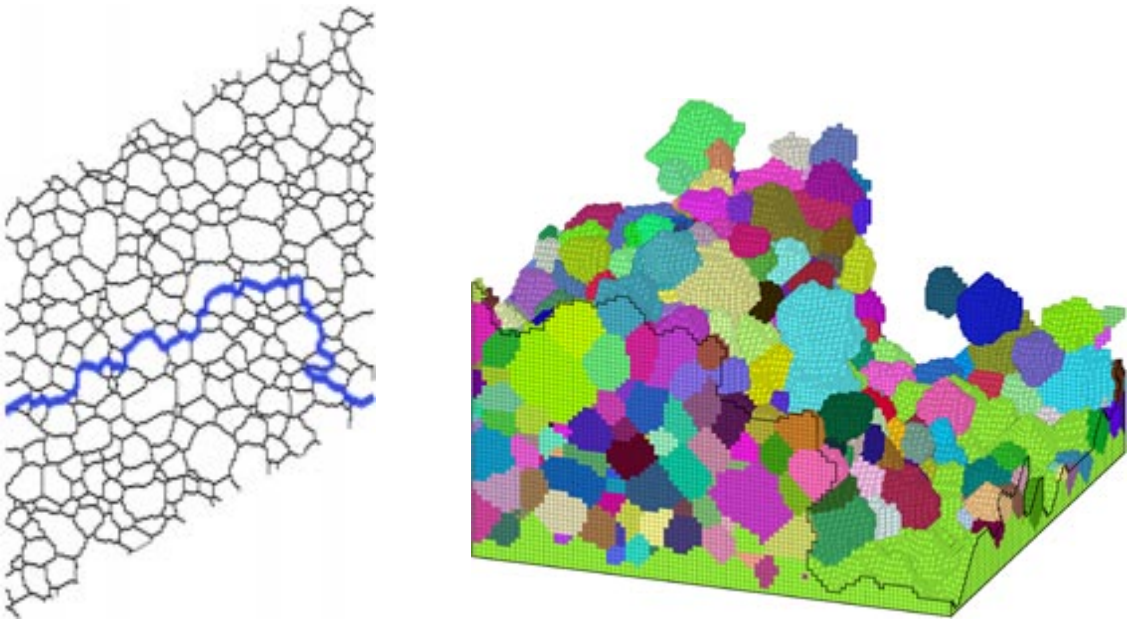

(a) (b)

Figure 6.4 - Intergranular fracture surface of minimum surface formation energy for equiaxed polycrystals. (a) 2D polycrystal with $f = 0.5$ very low surface formation energy boundaries (microcracks). (b) 3D polycrystal with $f = 0.8$. Note the convoluted fracture surfaces, which include geometrically interlocking grains.

Because the special boundaries break easily, the fracture surface deviates in order to include them, as shown in Figure 6.4. These deviations may lead to geometrically interlocking grains, so that although the system is "broken" it cannot be separated into two pieces without further fracture. The minimum energy fracture area increases, with a peak near $f = 0.5$ in 2D and $f = 0.8$ in 3D, as shown in Figure 6.5. These maxima indicate percolation thresholds for microcracked boundaries. In 2D, this is a traditional percolation threshold, where a continuous path of microcracked boundaries spans the sample. In 3D, however, this threshold corresponds to the formation of a continuous 2D surface of microcracked grain boundaries. Such higher-dimensional percolation problems are computationally challenging; in fact, the max-flow/min-cut algorithm used here is an efficient way to attack them.

6.5 CONCLUSIONS

Network optimization algorithms allow efficient determination of the minimum surface formation energies and surfaces for intergranular fracture in 2D and 3D polycrystals. For equiaxed grains and uniform boundary strength, fracture surfaces are relatively smooth with no interlocking grains. The minimum energy fracture area is independent of grain size and is 10% larger than the specimen cross-section in 2D and

45% larger in 3D. The 3D fracture area is larger than projected from 2D systems, indicating that the propagation of linear and planar cracks is fundamentally different. In systems with microcracked boundaries, the fracture surface deviates to preferentially include microcracked boundaries, allowing interlocking grain configurations. Percolation of microcracks occurs at about 50% microcracked boundaries in 2D and 80% in 3D.

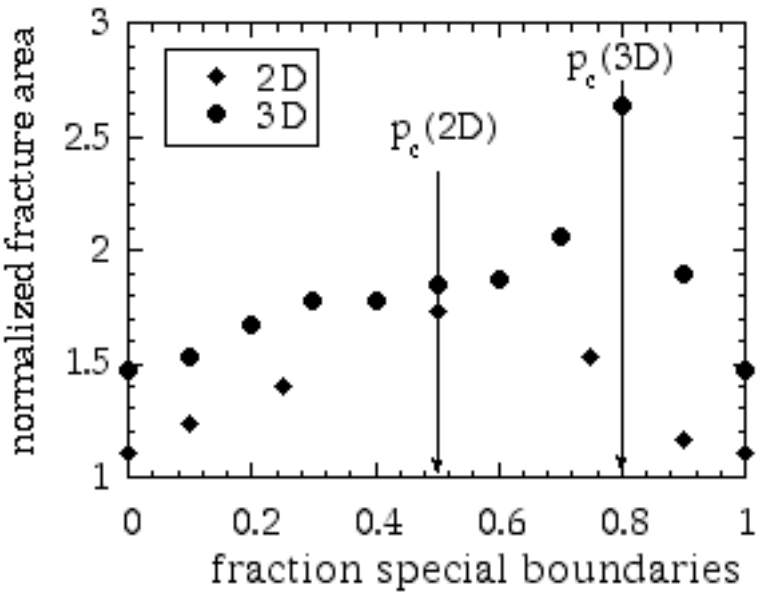

Figure 6.5. Normalized intergranular fracture surface size as a function of fraction microcracked boundaries in 2D (diamonds) and 3D (circles). The maximum surface area fracture occurs at the percolation threshold for microcracks, p_c.

6.6 FUTURE WORK

Many polycrystalline materials fracture in a mixed trans- and intergranular mode. Network optimization algorithms have been extended to characterize mixed mode fracture. Results indicate a first-order phase transition between cleavage and intergranular fracture.

Moreover, a number of other microstructural phenomena can be formulated as network optimization problems. Future work will include investigations of the utility of network optimization approaches to microsystems, as shown in Table 6.1.

Table 6.1 - Microsystems applications of network optimization algorithms.

Phenomenon	Application
fracture of polycrystalline materials	failure prediction for LIGA components
liquid infiltration by capillarity into a complex geometry	microsensors, lubrication of MEMS devices
dislocation or microcrack cluster size analysis	spallation in MEMS devices
cascade network identification	plastic deformation in LIGA components

6.7 REFERENCES

6.1 T. H. Cormen, C. E. Leiserson, and R. L. Rivest, *Introduction to Algorithms* (McGraw-Hill Book Company, New York, 1990) pp. 527-531.

6.2 L. R. Ford Jr., D. R. Fulkerson, *Flows in Networks* (Princeton Press, Princeton, NJ, 1962).

6.3 J. Edmonds, R. M. Karp, *JACM* **19**[2] 248 (1972).

6.4 M. P. Anderson, D. J. Srolovitz, G. S. Grest, P. S. Sahni, *Acta Metall.* **32**[5] 783 (1984).

6.5 D. J. Srolovitz, M. P. Anderson, P. S. Sahni, G. S. Grest, *Acta Metall.* **32**[5] 793 (1984).

6.6 M. P. Anderson, G. S. Grest, D. J. Srolovitz, *Phil. Mag. B* **59**[3] 293 (1989).

6.7 R. E. Reed-Hill, *Physical Metallurgy Principles*, 2nd edition (Brooks/Cole Engineering Division, Monterey, CA, 1973) p. 220.

6.8 E. A. Holm, *J. Amer. Ceram. Soc.* **81**[3] 455 (1998).

6.9 E. A. Holm, G. N. McGovney, *Mat. Res. Soc. Symp. Proc.* **539** 325-330 (1999).

Distribution

5	MS1056	1111	J.A. Knapp
1	MS1056	1111	B.L. Doyle
1	MS1080	1769	J.L. Dohner
5	MS1080	1749	M.P. de Boer
1	MS1411	1834	E.A. Holm
1	MS1411	1834	H.E. Fang
1	MS0319	2613	C.W. Vanecek
1	MS0329	2614	G.E. Sleefe
1	MS0329	2614	F. Bitsie
1	MS0329	2614	F.J. Peter
1	MS0329	2614	D. Hoke
1	MS9042	8725	B.R. Antoun
1	MS9405	8726	D. Bammann
1	MS9161	8726	E.P. Chen
1	MS9161	8726	R. Jones
1	MS0841	9100	T.C. Bickel
1	MS0824	9110	A.C. Ratzel
1	MS0826	9113	W.L. Hermina
5	MS0826	9113	C.C. Wong
5	MS0826	9113	E.S. Piekos
1	MS0834	9114	J.E. Johannes
1	MS0827	9117	M.A. Gallis
1	MS0847	9120	H.S. Morgan
1	MS0893	9123	R.M. Brannon
5	MS0893	9123	E.D. Reedy
1	MS0847	9124	Manager
5	MS0847	9124	J.M. Redmond
1	MS0847	9124	K.F. Alvin
1	MS0847	9124	O.B. Ozdoganlar
1	MS0557	9125	T.J. Baca
1	MS0847	9125	J.E. Freymiller
1	MS0847	9126	R.A. May
1	MS0835	9140	J.M. McGlaun
1	MS0847	9142	J.A. Mitchell
1	MS0835	9142	J.S. Peery
5	MS0847	9142	M.W. Heinstein
1	MS9018	8945-1	Central Technical Files
2	MS0899	9616	Technical Library
1	MS0619	9612	Review &Approval Desk

1 Professor R.W. Carpick
Engineering Physics Department
University of Wisconsin – Madison
1500 Engineering Drive
Madison, WI 53706-1687

1 Professor M.L. Dunn
Department of Mechanical Engineering
427 UCB
University of Colorado
Bolder, CO 80309-0427